

Ferric sulfates on Mars: A combined mission data analysis of salty soils at Gusev crater and laboratory experimental investigations

Alian Wang¹ and Z. C. Ling^{1,2}

Received 28 May 2010; revised 22 November 2010; accepted 21 December 2010; published 4 March 2011.

[1] A temporal visible near-infrared (VIS-NIR) spectral variation was observed from Tyrone yellowish salty soils based on seven periodic Pancam 13 filter observations made by the Spirit rover. The major change was the reduction of spectral slope from 434 nm to 753 nm. Based on the results from a set of systematic laboratory experiments on the stability field and phase transition pathway of typical ferric sulfates, we suggest that the strong dehydration processes of ferricopiapite, either through amorphization or chemical alteration, could be the reasons for the spectral changes of Tyrone yellowish salty soils, excavated from a deep trench. The change of soil property suggests that they were originally not in equilibrium with the surface atmospheric conditions, that there is a relative humidity (RH) gradient existing in the upper few tens of centimeters depth below the surface. A layer of salt-rich regolith beneath the surface will change the underground temperature profile, especially to keep a low-temperature zone with a small temperature oscillation (than diurnal cycle at surface) in a salt-enriched regolith layer. This temperature profile will provide a relatively high RH and small RH variation and thus will facilitate the preservation of hydrous sulfates with high degree of hydration during the moderate obliquity period on Mars. Additionally, the sulfates with high degrees of hydration are excellent RH buffers in a local environment. The subsurface hydrous sulfates can be the sources for high level of water-equivalent hydrogen found at two large equatorial regions on Mars by Neutron Spectrometer on Mars Odyssey Orbiter.

Citation: Wang, A., and Z. C. Ling (2011), Ferric sulfates on Mars: A combined mission data analysis of salty soils at Gusev crater and laboratory experimental investigations, *J. Geophys. Res.*, 116, E00F17, doi:10.1029/2010JE003665.

1. Introduction

[2] Sulfate is one of the major types of secondary minerals found on Mars by recent missions, which reinforces its importance for Mars science. Sulfates are excellent hosts of water [Chipera and Vaniman, 2007; Chou and Seal, 2007; Vaniman et al., 2004; Vaniman and Chipera, 2006; Wang et al., 2009a, 2009b], the sinks of acidity [Tosca et al., 2004], and may be the most active species in the past and current surface/near-surface processes on Mars [Chevrier and Altheide, 2008; McLennan et al., 2007]. These processes involve both igneous rocks (mainly basalts [McSween et al., 2004, 2006, 2008]) and sedimentary materials, e.g., phyllosilicate-bearing deposits [Bishop et al., 2008; Ehlmann et al., 2008a; Mustard et al., 2008] and even carbonates [Ehlmann et al., 2008b].

[3] One of the mysteries in Martian sulfate observations is the detections by the two Mars Exploration Rovers (MER)

of jarosite in Meridiani outcrop [Klingelhöfer et al., 2004] (widely spread over hundreds kilometers) and the variety of ferric sulfates within the subsurface regolith at Gusev crater [Morris et al., 2006, 2008], in comparison with the rarity of findings of Fe-sulfates by orbital remote sensing, even over Meridiani Planum [Wiseman et al., 2007]. By remote sensing, Mg- and Ca-sulfates were identified with a wide vertical and horizontal spread in Valles Marineris, Meridiani Planum, and the North Polar Region by the OMEGA team [Arvidson et al., 2005; Bibring et al., 2005; Gendrin et al., 2005; Langevin et al., 2005] and by CRISM team [Murchie et al., 2007; Roach et al., 2008]. In contrast, only a few occurrences Fe-sulfates were reported by CRISM team [Lichtenberg et al., 2009, 2010; Milliken et al., 2007a, 2007b, 2008, 2009; Roach et al., 2007, 2008, 2009a, 2009b, 2009c], while the overall quantity of Fe-sulfates at the potential occurrences is not comparable with those of Mg- and Ca-sulfates.

[4] Using its nonfunctional right front wheel as a trenching tool, the Mars Exploration Rover Spirit is continuing excavating and identifying a variety of sulfates (ferric sulfates and Ca-, Mg-sulfates) and other secondary minerals (silica) at various locations in Gusev crater. Eight more locations (Figure 1) were found after the 10 locations reported previously by Athena team [Haskin et al., 2005; Johnson et al., 2007; Rice et al., 2009; Wang et al., 2006a, 2006b, 2008]. More

¹Department of Earth and Planetary Sciences and McDonnell Center for Space Sciences, Washington University, St. Louis, Missouri, USA.

²School of Space Science and Physics, Shandong University, Weihai, China.

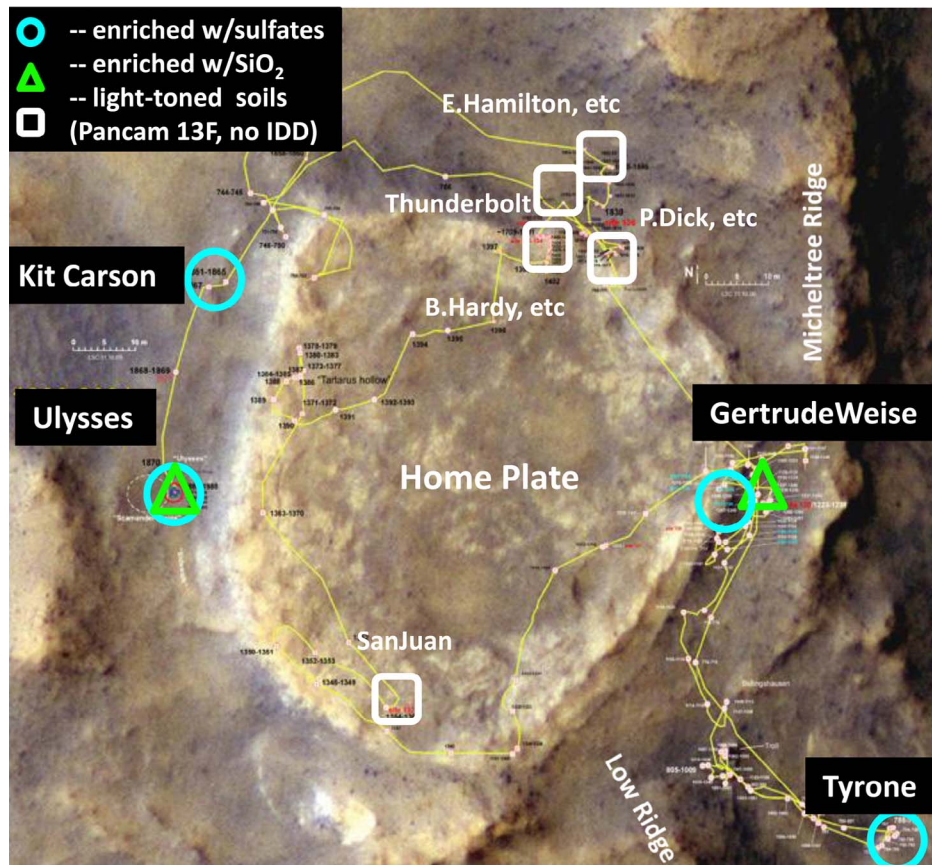


Figure 1. Light-toned soil patches found by the Spirit rover around Home Plate.

importantly, a potential phase transformation of sulfates was observed after their exposure under current Martian surface atmospheric conditions, within the salty soils at Tyrone (east of Home Plate [Wang *et al.*, 2008]), and potentially within the salty soils at Kit-Carson and at Troy (west of Home Plate [Arvidson *et al.*, 2010; Rice *et al.*, 2011]). These discoveries, if verified, would provide the evidence for a set of different environmental conditions, temperature (T), and relative humidity (RH), existing within the shallow subsurface on Mars.

[5] In this paper, we conduct a detailed study of the visible near-infrared (VIS-NIR) spectra extracted from a set of seven periodic 13 filter (13F) Pancam observations from Tyrone salty soils through 198 sols. We then use the results from a set of systematic experimental studies on the stability field and phase transition pathways of ferric sulfates to determine the potential causes of temporal spectral variations of Tyrone yellowish salty soil.

2. Tyrone Salty Soils

[6] Tyrone salty soils have three extremely interesting characteristics. First, they occur within a local topographic low, and near some Si-rich materials. The Tyrone site (Figure 1) is within a triangular-shaped low marked by the 45.0 m contour line, surrounded by Low Ridge (about 4 m higher), Home Plate (about half meter higher), and Mitcheltree Ridge (about 1 m higher). It is important to mention

that light-toned, Si-rich soils and Si-rich nodular materials were also identified within the same topographic low where Tyrone S-rich salty soils were excavated. Extensive investigations were made by the Spirit rover on these materials during its exploration on the floor of Eastern Valley between Mitcheltree Ridge and the east side of Home Plate [Arvidson *et al.*, 2008; Lewis *et al.*, 2008; Ming *et al.*, 2008; Morris *et al.*, 2008; Schmidt *et al.*, 2008; Squyres *et al.*, 2008; Wang *et al.*, 2008].

[7] Second, Tyrone salty soils are characterized by a two-layer structure and a homogeneous spatial distribution of salty soils within each layer (described as whitish and yellowish soil layers separately), which is distinctly different from the salty soils at other locations excavated by the Spirit rover (e.g., at Dead Sea and Paso Robles). The two-layer structure of salty soils at Tyrone was demonstrated by a combined Pancam and Navcam images analysis; that is, the whitish salty soil occur in the shallow tracks made by five normally rolling wheels of the Spirit rover and the yellowish soils occur only in the deeper trench made by the non-function right front wheel [Wang *et al.*, 2008, Figure 26], suggesting that yellowish salty soils were excavated from subsurface at a deeper depth than whitish salty soil. The homogeneity of each layer can be seen in Figure 2. Figure 2a is a false color Pancam image of Tyrone soils (sol 790-P2531 means a Pancam observation sequence 2531 taken in sol 790), with the region of interest (ROIs) (from where the spectra were extracted) marked by solid colored squares. The

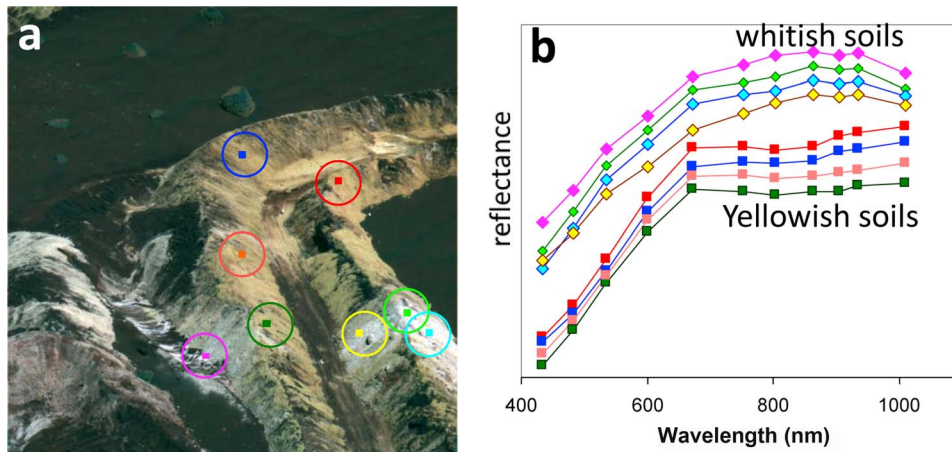


Figure 2. Pancam observation (sol 790-P2531) using 13 geologic filters when the Spirit rover stopped at Tyrone site (~ 3.2 m from excavated salty soil). (a) False color image with ROIs marked as small rectangles. The Vis-NIR spectra were extracted from those ROIs, and (b) VIS-NIR spectra were extracted from Tyrone salty soil patches (ROIs). Colors of spectra correspond to the colors of the rectangles in Figure 2a. All spectra were shifted in reflectance in order to group those from whitish soil patches (top four spectra) and those from yellowish soil patches (bottom four spectra). A similarity in the spectral pattern of each soil type can be seen very clearly, which demonstrated a mineral and chemical homogeneity in each layer, as reflected in 0.4 to 1.0 μm VNIR reflectance spectral region. The width of the trench is slightly wider than the width (16 cm) of the Spirit rover wheel.

VIS-NIR reflectance spectra extracted from the multicolor Pancam image cube are shown in Figure 2b. A similarity in the spectral pattern of each soil type can be seen very clearly, i.e., the top four spectra from whitish soil patches and the bottom four spectra from yellowish soil patches. These spectra demonstrate the mineral and chemical homogeneity in each layer, as reflected in 0.4 to 1.0 μm VIS-NIR reflectance spectral region.

[8] The spectral characteristics of yellowish soils include a steeper slope from 434 nm to 673 nm, a convex shape in visible spectral range with a shallow absorption band centered near 803 nm. The spectral characteristics of whitish soils include a generally higher albedo, a concave shape in visible spectral range with a negative spectral slope from 934 nm to 1009 nm in IR range. The spectral differences of two types of Tyrone salty soils are large enough that the R^* values from them appear as two well-separated branches of data points in the two-dimensional filter histograms: Figure 3a for R^* (L2 filter, centered at 753 nm) versus R^* (L7 filter, centered at 432 nm) and Figure 3c for R^* (R7 filter, centered at 1009 nm) versus R^* (R1 filter, centered at 436 nm). In these 2-D histograms, the top right branched portion of data cloud corresponds salty soils, with upper branch corresponds yellowish salty soils and lower branch corresponds whitish salty soils. All pixels from salty soils have higher R^* values than the surrounding basaltic soils (disturbed and nondisturbed surface soils), which are represented by the lower left dense portion of data cloud in Figure 3.

[9] The Pancam stereo camera on the Spirit rover has two eyes (left and right eyes, marked as L and R) using two 1024 by 1024 active area charge-coupled devices (CCDs) with a 30 cm stereo separation and a 0.27 mrad per pixel resolution [Bell *et al.*, 2003]. Each eye of the camera is covered by an eight position filter wheel, with 13 filters used for multi-

spectral geologic investigations. Two pairs of filters are common between both eyes, leaving 11 unique wavelengths (image taken through a filter is marked as Lx or Rx, where x annotates the specific filter). Multispectral data from images of the onboard calibration target were used in combination with prelaunch calibration information to convert raw image data to calibrated radiance and then to radiance factor IOF (I/pF , where I is the measured radiance and pF is the incident solar irradiance) [Bell *et al.*, 2003, 2006]. Accumulation of air fall dust on the calibration target over the course of the mission was corrected using a two-layer Hapke model along with the known photometric properties of the calibration target [Bell *et al.*, 2006; Sohl-Dickstein *et al.*, 2005]. The IOF data were converted to relative reflectance (R^*) (where R^* is defined as IOF divided by the cosine of the solar incidence angle [Bell *et al.*, 2006; Reid *et al.*, 1999]). Bell *et al.* [2006] estimated filter-to-filter uncertainties in R^* of 1%–5%, providing confidence in the reality of even very small-scale spectral variations detected in the scene. For all VIS-NIR spectra extracted from multispectral Pancam images in this study, relative reflectance R^* was used.

[10] Figure 3b is a 3-D filter histogram, in which the color scale represents the appearance frequencies of the data points at particular R^* (L2) versus R^* (L7) pair values in the plotted range. It demonstrates that the central zone in each of the two data branches of Tyrone salty soils has the highest data populations. This property will be used in the selection of ROIs for extracting the representative spectra for whitish and yellowish salty soils (section 2.1.1).

[11] Third, it was observed that Tyrone yellowish salty soils demonstrated a property change after being exposed under current Mars surface atmospheric conditions [Wang *et al.*, 2008]. The details in those property changes will be discussed in section 2.1.

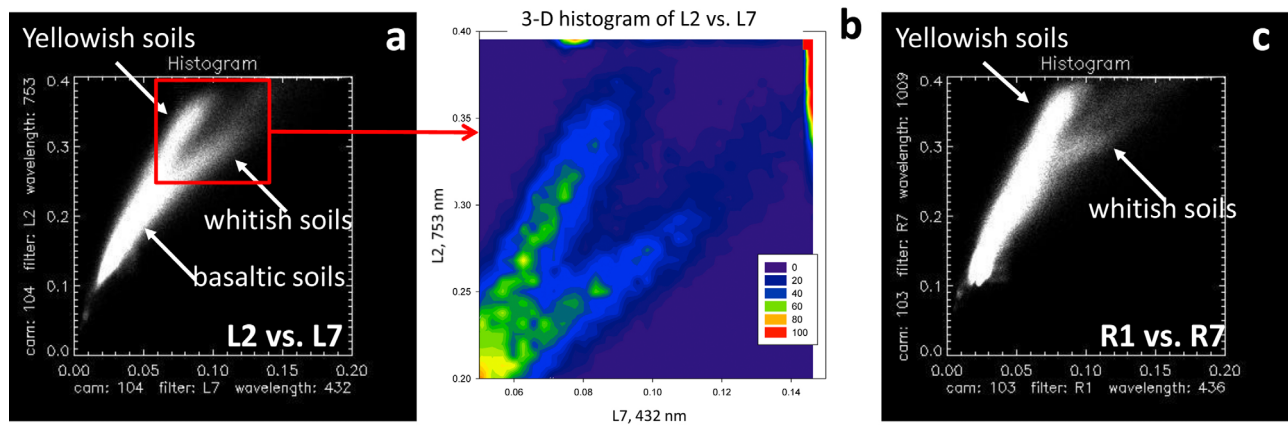


Figure 3. Histograms from Pancam sol 790-P2531 observation (at Tyrone site, ~ 3.2 m from excavated salty soils). (a) Two-dimensional histograms of L2 versus L7 (i.e., 753 nm versus 432 nm) using R^* of each pixel in two Pancam images. The data from yellowish and whitish salty soils appear as two well-separated branches at top right portion of this histogram. (b) Three-dimensional histogram of L2 versus L7, where the color scale represents the appearance frequencies of the data points at particular $R^*(L2)$ versus $R^*(L7)$ pair values in the plotted range. It shows the “central zone” in each data branch is highly populated. (c) Two-dimensional histogram of R1 versus R7, in which the data points from yellowish and whitish salty soils appear as two well-separated branches as well.

2.1. Temporal Change in the VIS-NIR Spectra of Tyrone Salty Soils

[12] After the exposure of Tyrone salty soils, the Spirit rover spent 283 sols (from sol 805 to sol 1088) on the slope of Low Ridge for its second winter campaign. During this period, seven sets of 13-filter Pancam observations were taken periodically of the Tyrone site (about 31 m away from Spirit winter campaign site). The purpose was to track the potential changes in VIS-NIR spectra of exposed salty soils under current Mars surface atmospheric conditions.

[13] The temporal property changes of Tyrone salty soils during this campaign were identified. It was done specifically by monitoring the two branches of data cloud in L2 (753 nm) versus L7(432 nm) 2-D filter histogram (Figure 4, the upper branch represents Tyrone yellowish salty soils while the lower branch represents Tyrone whitish salty soils). This observational methodology poses high statistical significance because (1) R^* from all 2×524288 pixels in each pair of Pancam images (through L2 and L7 filters) are plotted and (2) the characters of each branch in the 2-D histogram are determined by the group behaviors of yellowish and whitish salty soils as the function of time. It means that the majority of pixels of each type of salty soils determined the orientations of data branch(s) in the histogram. In addition, they are not influenced by the basaltic soils that were physically mixed with the salty soils at Tyrone site, because the pixels from basaltic soils only occur at the lower left dense portion of data cloud (Figures 3 and 4).

[14] Figures 4a–4g show the R^* (L2, 753 nm) versus R^* (L7, 432 nm) 2-D histograms from seven Pancam 13 filter observations taken from Low Ridge during sol 864 to sol 1062 time period. The major difference among the seven histograms is directly observable; that is, the separation between the two branches was reduced following the increased time durations of exposure from 80 sols (since sol 784 when Tyrone salty soils were first excavated until sol

864) to 278 sols (until sol 1062). Figure 4h shows the approximate changes in the orientations of two data branches of sol 1062-P2596 observation from those taken in sol 864-P2547. Because the positions of two branches in this 2-D histogram represent the group behaviors of two types of Tyrone salty soils, the reduction in branch separation suggests a bulk change in spectral property has happened (where bulk indicates the majority of salty soils of specific type, yellowish or whitish). Figure 4h indicates that the reduction in branch separation is primarily caused by a decrease in the blue-to-red spectral slope of the yellowish soils, while the corresponding spectral slope of the whitish soils does not appear to have changed with time.

2.1.1. Extracting Representative VIS-NIR Spectra From Two Types of Tyrone Salty Soils

[15] Figure 4 reveals an overall view on a bulk change in spectral property of Tyrone salty soils. This overall view carries the highest statistical significance, because it is a simply plot of R^* values from all pixels (2×524288) in each of the seven studied Pancam observations (without further data handling other than the initial data calibration). The goal of current study is to search for the mineralogical and chemical causes for this spectral change. For that purpose, we have to extract the VIS-NIR spectra from the multicolor Pancam image cubes of seven observations. During these spectral extraction processes, it is critical to carry the statistical meaning as much as possible, while understanding that the statistics will naturally get worse if compared with the overall view of Figure 4, because of the uncertainties added during the data handling processes.

[16] During the data processing, the selection of sampling areas (ROIs) for spectra extraction is critical. In order to keep the extracted spectra to be statistically as meaningful as possible, the essential rule 1 is that each ROI should contain ONLY the pixels from an individual type of soils. In this study, we deal with four types of soils, undisturbed surface

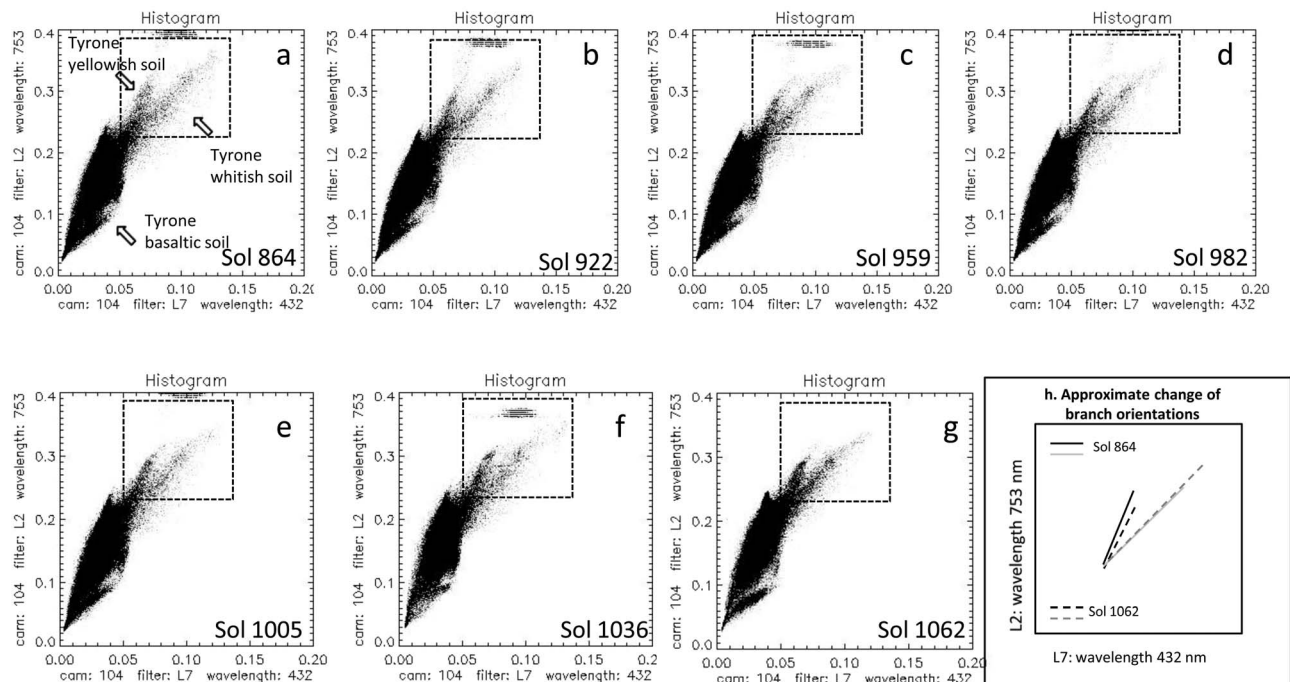


Figure 4. Data from seven 13F Pancam observations taken about 31 m away from Tyrone site when Spirit rover parked at Low Ridge. The R^* values of all pixels in two Pancam images taken through L2 (753 nm) and L7 (432 nm) filters from seven 13F Pancam observations were plotted in these 2-D histograms. The two branches of data points (approximately enclosed in a dashed line square) in each histogram represent Tyrone yellowish salty soil and Tyrone whitish salty soil, respectively. (a–g) Seven histograms show a trend of reduction in the separation of two branches following the increase of time duration when the Tyrone salty soils were exposed to the surface atmospheric conditions at Gusev, Mars. (h) An estimated approximate change in branch orientations from sol 864 to sol 1062.

soil, disturbed basaltic soil in rover tracks, the whitish salty soil from shallow subsurface regolith, and the yellowish salty soil from the deep trench.

[17] Figure 5a shows that the selections of ROIs for undisturbed surface soils and for disturbed basaltic soils in rover tracks can be made very straightforwardly in the Pancam images through L2 filter (two rectangles with red and blue colors in Figure 5a). The locations of these ROIs are chosen quite far away from excavated salty soils, and also far away from each other. Even in the images taken at 31 m away (when the Spirit rover parked on Low Ridge), the albedo of surface soils and disturbed soils in tracks are so different, that no mixing of other types of soils would be included in either of these two ROIs. Furthermore, we have chosen the ROI for nondisturbed soils at the exact same location and having the exact same size in each L2 image from the seven periodic Pancam 13F observations (same for the ROI selection of disturbed basaltic soils), thus we can use the extracted spectra to monitor the effects of instrumental and atmospheric condition changes (discussed in section 2.1.3).

[18] In contrast, the selection of ROIs for yellowish and whitish salty soils cannot be done in the same way. At Tyrone site, the physical mixing of basaltic soils with the light-toned salty soils and the physical mixing between yellowish and whitish soils are very obviously seen in the image taken when the Spirit rover standing right next to the excavated salty soils (Figure 2a). Different from *Rice et al.*

[2011], we believe that it is thus impossible to draw the boundary between Tyrone whitish and yellowish salty soils in a Pancam image taken at 31 m away from Tyrone site (when the Spirit rover parked on Low Ridge), for the purpose of selecting their ROIs. If a chosen ROI of yellowish soils contains the pixels of basaltic soil or whitish soil, the extracted spectrum from this ROI would represent a soil mixture. Any further analysis using such extracted spectra (of mixtures) will undoubtedly diminish the statistical significant spectral change revealed by the overall view of Figure 4.

[19] Instead of using spatial boundaries in an image, we choose to use the spectral characters of each type of salty soils as criteria for the selection their ROIs. For example, to ensure the ROI for Tyrone yellowish salty soils contains ONLY the pixels of yellowish soils, we select its ROI from the upper branch in L2 versus L7 2-D filter histograms, and ROI for whitish soils from the lower branch in L2 versus L7 2-D filters histograms (Figure 5b). By doing so, the basaltic soils that physically mixed with Tyrone light-toned salty soils would not be included in either ROIs. In addition, the pixels from whitish soil would not be included in the ROI of yellowish soils, and vice versa. Given the nature of salty soils occurrence at Tyrone, this methodology provides the only way to satisfy the essential ROI selection rule 1.

[20] Additional to the essential rule 1, in order to carry the statistical significant spectral change (revealed by the overall view of Figure 4) through the spectra extraction processes,

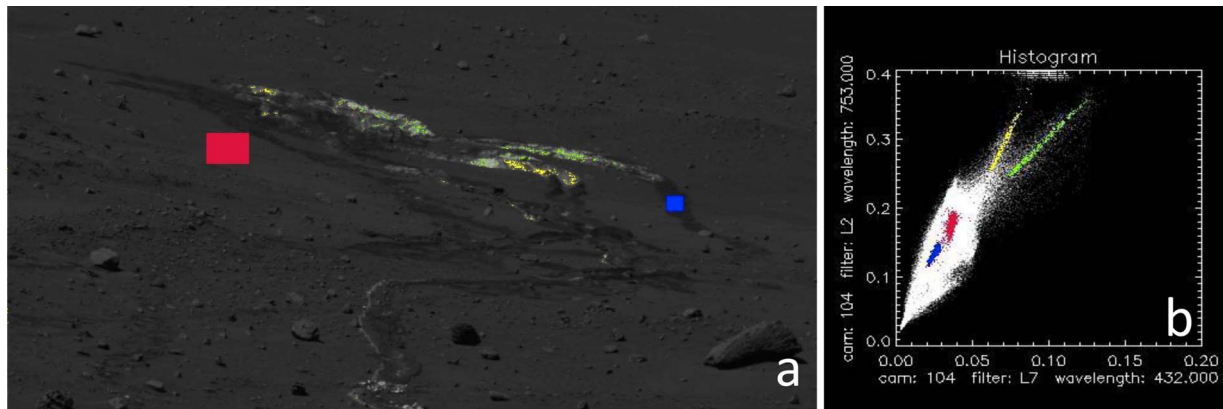


Figure 5. The selections of ROIs for seven 13F Pancam observations taken about 31 m away from Tyrone site when Spirit rover parked at Low Ridge. (a) The ROIs for nondisturbed surface and disturbed basaltic soils were selected from L2 image of each of seven observations (at exactly the same locations and the same sizes in seven L2 images). (b) The ROIs for typical yellowish and whitish salty soils were selected from L2 versus L7 2-D filter histograms for each of seven observations, as an elongated zone along the central line of the data branch that represent only the typical yellowish (or whitish) salty soils, with $\Delta R^* \sim 0.05$ as the zone width and with $R^*_{L2} > 0.25$. The corresponding locations of the ROIs for salty soils in Pancam L2 images are shown in Figure 5a, while the corresponding locations of ROIs for basaltic soils in 2-D histogram are shown in Figure 5b.

the selected ROIs for Tyrone salty soils must (2) contain large enough number of pixels and (3) represent the trend of changes (the overall view) revealed by Figures 4a–4g. The first requirement asks for as much data points as possible to be included. The second requirement asks to exclude outliers. In order to satisfy both requirements, we choose the ROI for each of the two salty soils to be an elongated zone along the central line of the corresponding data branch in L2 versus L7 2-D histogram. In addition, a width of $\Delta R^* \sim 0.05$ was used to draw the zones of ROIs, and only the pixels with R^*_{L2} (753 nm) values > 0.25 was used to avoid the potential mixing of the data from whitish and yellowish soils (Figure 5b). As revealed by the 3-D histogram of Figure 3b, the central zone of each data branch is the most populated region by the data for either yellowish or whitish salty soils. A ROI taken at central zone of the data branch will first include a large number of pixels and is statistically meaningful (rule 2). Second, the densely populated central zones can best express the trend of change (the overall view) as function of time, i.e., the reduction of branch separation shown in Figures 4a–4g. Thus the selection of branch central zones for ROIs of two salty soils will satisfy ROI selection rule (3) as well.

2.1.2. Comparing the Spectra Taken at 31 m Distance With Those at 3.2 m

[21] Before making a comparison among the extracted spectra of seven periodic Pancam 13F observations taken at Low Ridge, we need to compare the basic spectral characters from the these observations (about 31 m away from the actual Tyrone site) with those taken at Tyrone site (Figure 2b, ~ 3.2 m from the center of excavated salty soils), in case there are changes caused by long-distance measurements.

[22] The extracted VIS-NIR spectra from the first (sol 864-P2531) of seven periodic Pancam 13F observations (taken at 31 m away) are shown in Figure 6. For each spectrum in Figure 6a, the position of a square symbol represents the mean R^* of a specific type of soils at a spe-

cific wavelength, the error bar represents the mean $R^* \pm$ STD (standard deviation of measured R^* values). The mean R^* and STD at a specific wavelength (x) are obtained from the measured R^* values of all pixels included in the selected ROI in a Pancam image through a specific filter (L_x) using MERTOOLS analysis, which is an IDL based software designed by MER-Pancam team. Alternatively in Figure 6b, the error bars represent the mean $R^* \pm$ STDOM (standard deviation of mean R^*). The STDOM was calculated in following way:

$$\text{STDOM} = [\text{STD} \cdot t] / \text{SQRT}(N) \quad (1)$$

where t is the Student's t test factor at 95% confident level, N is the number of pixels included in a ROI. The relative positions of the mean R^* values at each wavelength and the size of STD or STDOM can be used to evaluate the statistical significance of the spectral features of four different types of soils.

[23] The STDs in the spectra of nondisturbed surface and disturbed basaltic soils (bottom two spectra in Figure 6a) are mostly equal or smaller than the size of mean R^* symbols, except at 753 nm where R^* from left eye (L2, 753 nm) and R^* from right eye (R1, 754 nm) of Pancam were averaged that increased the uncertainties slightly. These small STDs imply that all pixels in the ROIs of two types of basaltic soils have very consistent spectral features. When using the number of pixels included in each ROIs (1484 pixels in the ROI of undisturbed surface soil and 493 pixels in the ROI of disturbed soil; Figure 5a) to calculate STDOMs at all wavelengths, they were found to be about ten times smaller than STDs, thus demonstrating that the variation ranges of mean R^* at 95% confident level is smaller than the symbols in Figure 6b.

[24] ROIs of light-toned salty soils were selected using a special method for this study (section 2.1.1), thus the number of pixels in these ROIs can only be estimated in the

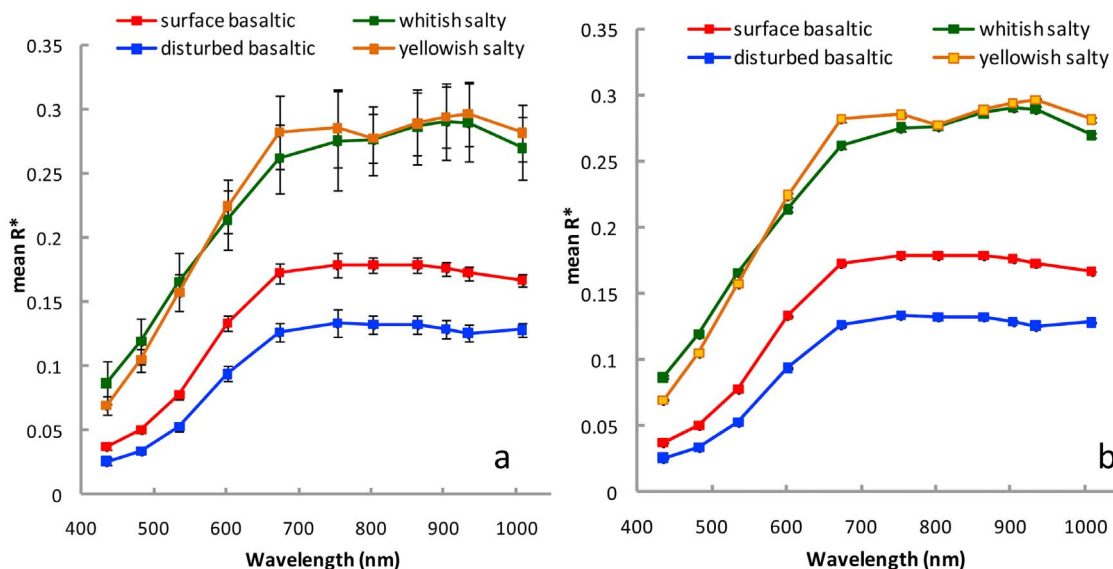


Figure 6. VIS-NIR spectra extracted from the first (sol 864-P2547) of seven Pancam 13F observations at Spirit winter campaign site (~31 m from Tyrone site). (a) Extracted mean R^* values with standard deviation. (b) Extracted mean R^* values with the standard deviation of the mean (STDOM). STDOMs show the very small variation ranges of mean R^* values at 95% confident level, due to the large number of pixels (>1000) included in each of selected ROIs.

following way. The seven periodic 13F Pancam Tyrone observations were all taken as half-frame images, except sol 1062-P2596. With a 1024×1024 CCD camera, there are 524288 pairs of data points in each of seven L2 versus L7 2-D histograms of Figure 4. Depending on the sol of measurement, there are about 8500 to 11500 pairs of data points in the upper right branched portion (i.e., $0.2 < R^*(L2, 753 \text{ nm}) < 0.5$ and $< 0.05 < R^*(L7, 432 \text{ nm}) < 0.2$) of these 2-D histograms, where ROIs of yellowish and whitish soils were selected. When selecting the ROIs as described in section 2.1.1, i.e., an elongated zone along the central line of each data branch, with $\Delta R^* = 0.05$ as zone width, and only including the pixels with $R^*(L2) > 0.25$ (Figure 5b), while keeping in mind the high data population in the central zones of branches (Figure 3b), a conservative estimate (e.g., 1/10) would suggest >1000 data pairs were included in each ROI of salty soils. Using 1000 as N in equation (1), the calculated STDOMs at all wavelength for yellowish and whitish soils have the sizes that are smaller than the symbol sizes of mean R^* in Figure 6b, which demonstrated the very limited variation ranges of the mean R^* values at 95% confident level. Therefore, although the sizes of STDs are generally larger in the spectra of salty soils than in the spectra of basaltic soils (with STDs in visible spectral range smaller than those at IR spectral range; Figure 6a), the large number of pixels included by their ROIs has raised the confident levels of all mean R^* values, which can ensure the reliability of the apparent spectral features of salty soils (Figure 6b).

[25] A comparison of top two spectra in Figure 6b suggests the following: (1) a higher albedo of whitish salty soils than yellowish soils at 434, 482, and 535 nm and (2) a high albedo of yellowish salty soils than whitish soils at 673 nm. Combining these two characters, the spectrum of yellowish

salty soils has a distinctly steeper spectral slope from blue to red. This character is clearly shown in the overall view of Figure 4, where the data branch belongs to yellowish soils is at the upper left side of the data branch of whitish soils, in all seven L2 versus L7 2-D histograms ($R^*_{753\text{nm}}$ versus $R^*_{432\text{nm}}$). The orientation of each data branch in these histograms actually corresponds to the spectral slopes from 434 nm (L7) to 753 nm (L2). Compared to the spectra in Figure 2b, we conclude that in visible spectral range, the spectral character of Pancam observations made at ~31 m away are consistent with that measured at Tyrone site (~3.2 m).

[26] On the other hand, in the IR range of the spectra extracted from the Pancam multicolor images taken at 31 m away from Tyrone site (Figure 6b), the spectral characteristics of both yellowish and whitish soils are different from those taken at Tyrone site. Namely when the observation was taken from a long distance, the typical characteristic spectral feature of yellowish soils appeared (in minor amount) in the spectra of whitish soils, and vice versa. For example, a very weak absorption “dip” centered near 803 nm (a spectral character of yellowish soils measured at Tyrone site; Figure 2b) appears in the spectra of whitish soils seen at ~31 m (Figure 6b); and the negative spectral slope from 934 to 1009 nm (a spectral character of whitish soils measured at Tyrone site; Figure 2b) appears in the spectra of yellowish soils seen at ~31 m (Figure 6b).

[27] Many reasons can cause the mixing of spectral characteristics in IR spectral range. The major influencing factor appears to be the long-distance measurements. Comparing with a Pancam image taken at Tyrone site (right side of Figure 7, in which the center of two Pancam “eyes” was at ~3.2 m from the center of excavated Tyrone salty soils), a ~31 m distance (left side of Figure 7) means a pixel

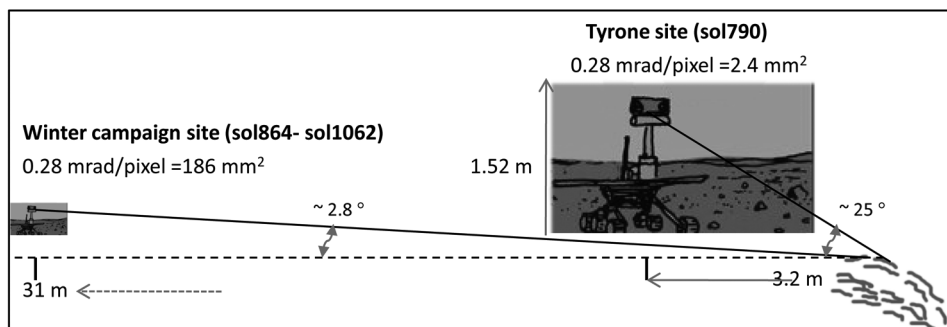


Figure 7. A scheme to show the difference in measurement geometry for the Pancam observations made at Tyrone site (where salty soils were at ~ 3.2 m from the Spirit rover) and for those made at Spirit winter campaign site (which was ~ 31 m from Tyrone site). In the latter case, the observations were made at a low viewing angle ($\sim 2.8^\circ$, compared with $\sim 25^\circ$ at 3.2 m), and the area covered by one pixel on Pancam CCD detector was ~ 80 times larger than the area/pixel when the measurement was made at 3.2 m. To observe an uneven surface at low viewing angle, the contribution from the solar radiation by single reflection is reduced; that is multiscattering can have higher contribution.

in Pancam CCD (0.28 mrad/pixel [Bell *et al.*, 2003]) would cover an area (1.4×1.4 cm, i.e., 186 mm^2) that is ~ 80 times of the area per pixel when the Spirit rover was at Tyrone site (2.4 mm^2). In a larger area covered by each pixel of Pancam CCD from 31 m away, the coexisting of yellowish and whitish soils (as seen in Figure 2a) can be the reason to cause the observed spectral mixing. In addition, aeolian activities during 74 sols (from sol 790 to sol 864) may move the grains of salty soils around, and to cause further coexistence of two salty soils in small spatial scale at Tyrone site.

[28] Another effect of long-distance observation is the change of viewing angle, an angle between the horizon and the line that connects the center of two Pancam “eyes” to the center of Tyrone salty soils. At 31 m away, the viewing angle is about 2.8° (Figure 7, sol 864 to sol 1062) in comparison with a much steeper viewing angle of $\sim 25^\circ$ at Tyrone site (sol 790). From a heavily disturbed surface like Tyrone site, the photons produced by direct reflections of solar radiation from the surface materials are more likely to be collected through a steep viewing angle (e.g., 25°) than a shallow viewing angle (e.g., 2.8°). In other word, multiscattering may have higher contribution to the measurements at 31 m away, thus could enhance the observed spectral mixing; that is, a portion of collected radiation by a low viewing angle may have experienced multiple scattering at different facets of a heavily disturbed area.

[29] Spectral mixing that can be caused by above reasons would happen in both VIS and IR spectral ranges, while a comparison of the spectra in Figures 6b and 2a suggests that it affects more the IR spectral range. The steeper spectral slope of yellowish salty soils in VIS spectral range can still be seen in Figure 6, and more importantly, Figures 4a–4g reveal that the difference in the spectral slopes (L2 versus L7, from 434 nm to 753 nm) of yellowish and whitish salty soils is statistically meaningful, when using the R^* values from all pixels.

[30] Because of the effective spectral mixing in IR wavelengths (>753 nm), only the spectral data in 434 nm to 753 nm range of seven periodic Pancam measurements taken at 31 m away will be used to evaluate the potential change of Tyrone salty soils through the second winter campaign of

Spirit rover. Nevertheless, the data in IR range will be used to monitor the potential development of physical mixing of salty soils (by aeolian process) through sol 784 to sol 1062.

[31] Note the spectral shape of nondisturbed basaltic soils (Figure 6) taken at ~ 31 m away is consistent with that taken at Tyrone site (~ 3.2 m [Wang *et al.*, 2008, Figure 23]). The spectral mixing with other type of soils is not apparent, mainly because these spectra were extracted from a ROI that is far away from excavated salty soils.

2.1.3. Temporal Spectral Variations

[32] In order to set up a reference to investigate the temporal spectral variation, VIS–NIR spectra of an undisturbed surface soil patch and a disturbed basaltic soil patch in a rover track from seven periodic Pancam 13F observations were plotted in Figure 8 (for which the mean $R^* \pm$ STDOMs are smaller than the line thickness of spectra, thus the error bars are not shown). They are extracted from the ROIs at same locations and of same sizes (Figure 5a) of all seven observations. With the exception of the spectra from sol 1062–P2596 (dashed line spectra), six spectra from a disturbed soil patch taken during 172 sols (sol 864 to sol 1036) overlap very well in general (bottom group of spectra in Figure 8).

[33] Six spectra from an undisturbed surface soil patch overlap well in visible wavelengths (top group of spectra in Figure 8), but show slight albedo changes in IR wavelengths (insert of Figure 8 shows the details). The top one in the solid line spectral group (insert of Figure 8) is from sol 982–P2566 and this at bottom is from sol 1036–P2585. There is a difference (ΔR^*) of 0.012 at 864 nm among six spectra. We notice that the tau values (a measure of atmospheric opacity) in the first five of this set of measurements have a median value of 0.345 and standard deviation of 0.033, and then increased to 0.514 in sol 1036. This tau increase may be the cause for the reduction of IR albedo for sol 1036–P2585 observation.

[34] The spectra extracted from the same undisturbed and disturbed soil patches in sol 1062–P2596 observation have generally higher albedo, because of a slightly different measurement condition. This measurement was made at the end of winter campaign when the Spirit rover moved to a

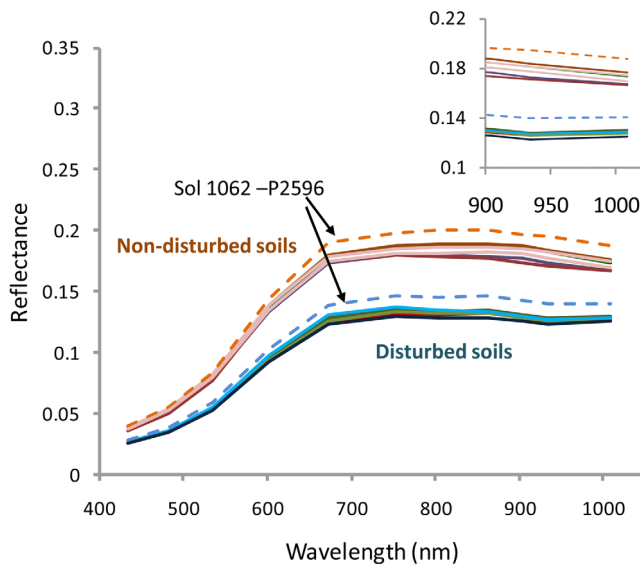


Figure 8. VIS-NIR spectra of nondisturbed surface and disturbed basaltic soils (ROIs taken at the same location and having the same size in each of seven L2 images), extracted from seven Pancam 13F observations from sol 864 to sol 1062 (~31 m away from Tyrone site). Except for the spectra of sol 1062-P2596 (dashed line spectra, taken from site 128, position 143), six spectra from a disturbed soil patch and a nondisturbed surface soil patch at different sols (solid line spectra, taken from site 128, position 0) overlap quite well in visible wavelengths. The albedo differences at IR wavelengths of the spectra (insert) from a nondisturbed surface soil patch may be caused by atmospheric dust settling during 172 sols. For example, the top one in the solid line spectral group of the insert was from sol 982-P2566, and the bottom one was from sol 1036-P2585.

different position (site 128 position 143, whereas six previous measurements from sol 864 to sol 1036 were made at site 128 position 0). The direct distance between the positions 0 and 143 of site 128 is only about 2–3 m, but the site azimuth angle toward Tyrone site has changed. In addition, There was a tau increase to 0.896 and a ~24% increase of solar elevation angle in sol 1062. All three factors can contribute to the albedo increases in the spectra of undisturbed and disturbed basaltic soils extracted from sol 1062-P2596 image cube. Based on Figure 8, data from sol 1062-P2596 will be excluded from our spectral comparison for salty soils.

[35] When plotting the spectra of Tyrone yellowish and whitish salty soils from the six periodic Pancam observations made from sol 864 to sol 1036, a slight albedo decrease was observed at all wavelengths (from 432 nm to 1009 nm) following the increase of exposure time duration, with some larger decreases at red IR wavelengths than those at blue-green wavelengths. The general decrease of albedo is consistent with the gradual dust settling on the surface of exposed light-toned salty soils during 172 sols' observation interval. In order to separate the potential spectral changes caused by other factors from the dust setting, we made slight upshift of the R^* values at all wavelengths by the same amount for the spectra of sol 922 to sol 1036, by forcing an equal R^* at 434 nm (L_7) for all six spectra (Figure 9).

Because the $R^* \pm$ STDs values at all wavelengths are smaller than the line thickness of the plotted spectra, the error bars are not visible in Figure 9. This general R^* value upshift does NOT remove all dust settling effect, which would have more contributions in red to IR spectral range. However, it facilitates the visual comparison of spectral shapes taken at different sols. Our discussion will concentrate on comparing the visible spectral range, especially the spectral slope from 434 nm to 753 nm, for the reasons discussed in section 2.1.2.

[36] A visual inspection suggests that six spectra from typical Tyrone whitish soils taken over 172 sols (Figure 9a) overlap quite well in 434 nm to 753 nm spectral range. The slightly different R^* values at red and infrared wavelengths contain the remaining (after the R^* upshift) effect of dust settling, which is more evident in the spectrum of sol 1036-P2858 when tau value dropped to 0.514 from 0.345 ± 0.033 of the first five observations. The shallow “dip” near 803 nm in some spectra of whitish soils comes from the spectral mixing discussed in section 2.1.2. The negative spectral slope from 934 nm to 1009 nm was recognized as characteristics of Tyrone whitish salty soils, an indicator for hydrous components in local S-rich and Si-rich species [Rice *et al.*, 2008, 2009; Wang *et al.*, 2008]. Among the six spectra in Figure 9a, the apparently nonchange in the negative spectral slope in 934–1009 nm range suggests a stable hydrous status of Tyrone whitish soils.

[37] The six spectra from typical Tyrone yellowish soils taken over a period of 172 sols (Figure 9b) show two changes: a reduction of spectral slope in 434–753 nm wavelength range, and a minor reduction of band depth centered near 803 nm, following the increase of time duration after the exposure of salty soils to current Mars surface atmospheric conditions. The apparently parallel six spectral segments in 934–1009 nm range of Figure 9b suggest that the physical mixing of salty soils (may partially caused by aeolian process) at Tyrone was not increased during the period (sol 864 to sol 1036), when 434–753 nm spectral slope experienced a decrease.

[38] In order to quantify these spectral changes, and to evaluate their statistical significances, four plots were produced and shown in Figure 10. They include, the spectral ratio of $R^*(L_2, 753 \text{ nm})/R^*(L_7, 434 \text{ nm})$ (Figure 10a), the spectral band depth of $(R^*(L_3, 673 \text{ nm}) + R^*(L_6, 934 \text{ nm}))/2 - R^*(L_3, 803 \text{ nm})$ (Figure 10b), the spectral slope of $(R^*(L_2, 753 \text{ nm}) - R^*(L_7, 434 \text{ nm}))/ (753 \text{ nm} - 434 \text{ nm})$ (Figure 10c), and the spectral slope of $(R^*(L_3, 673 \text{ nm}) - R^*(L_7, 434 \text{ nm}))/ (673 \text{ nm} - 434 \text{ nm})$ (Figure 10d). The STDs (of spectral ratio, spectral band depth, and spectral slopes) in these plots are obtained by propagations from the STDs of R^* in originally extracted spectra.

[39] When deriving the spectral ratio (Figure 10a), i.e., $R^*(L_2, 753 \text{ nm})/R^*(L_7, 434 \text{ nm})$, the following propagation of STDs was used:

$$\text{STD}(R_{L_2}^*/R_{L_7}^*) = (R_{L_2}^*/R_{L_7}^*) * \left[(\text{STD}_{L_2}/R_{L_2}^*)^2 + (\text{STD}_{L_7}/R_{L_7}^*)^2 \right]^{1/2} \quad (2)$$

which produces quite large STDs relative to the small variations in spectral ratio, and made these variations to be statistical meaningless (a consistent conclusion with that of

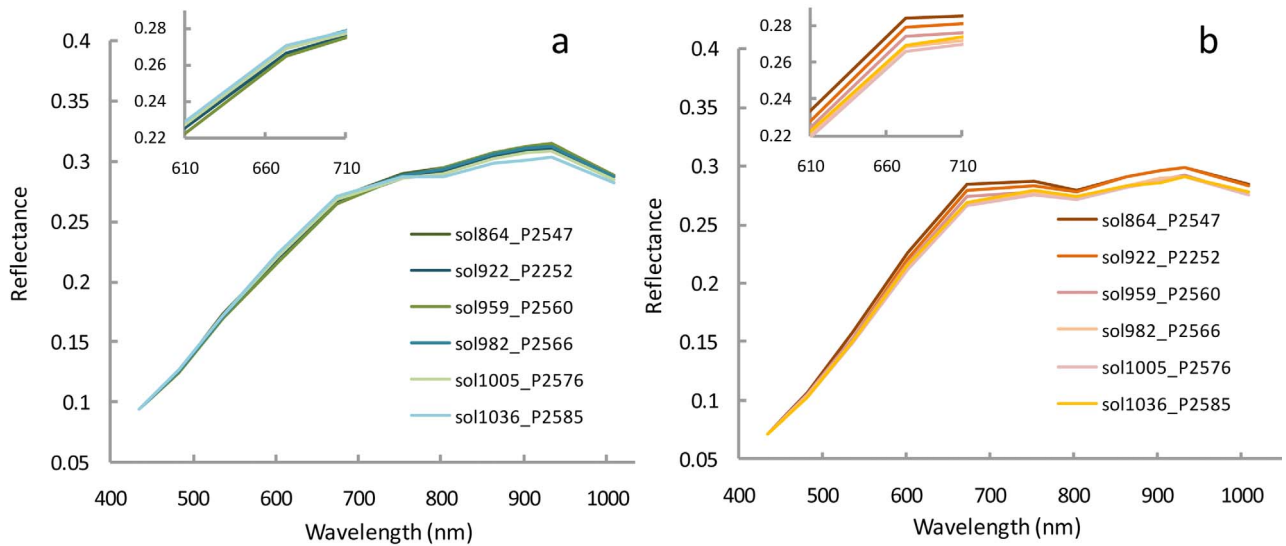


Figure 9. VIS-NIR spectra extracted from 13F Pancam images during the six Tyrone monitoring observations (from sol 864 to sol 1036, ~31 m away). (a) Tyrone whitish salty soils and (b) Tyrone yellowish salty soils. Details in 610–710 nm wavelength range are shown in the inserts. A slight albedo decrease as function of time was observed at all wavelengths (from 432 nm to 1009 nm) in the spectra of both salty soils (with smaller decreases in blue-green wavelength than those in red IR wavelength), consistent with the gradual dust settling on the surface of exposed light-toned salty soils during 172 sols’ observation interval. In order to separate the potential spectral changes caused by other factors from the dust setting, slight upshift of the R^* values at all wavelengths by the same amount were made for observations of sol 922 to sol 1036, in order to force an equal R^* at 434 nm (L7) for all six spectra. This method does not remove all dust settling effect (which would have more contributions in red and IR spectral range) but will facilitate a visual comparison of spectral shape.

Rice et al. [2011]). A similar conclusion can be drawn from spectral band depth calculation (Figure 10b), i.e., $(R^*(L3, 673 \text{ nm}) + R^*(R6, 934 \text{ nm}))/2 - R^*(R3, 803 \text{ nm})$, the small values of band depth and the very large STDs lower the statistical significance of band depth variations. When plotting the spectral ratio (or band depth) \pm STDOM (not shown), the same conclusions would be drawn even with the smaller error bars.

[40] For the calculation of spectral slopes, i.e., $(R^*(L2, 753 \text{ nm}) - R^*(L7, 434 \text{ nm}))/ (753 \text{ nm} - 434 \text{ nm})$ or $(R^*(L3, 673 \text{ nm}) - R^*(L7, 434 \text{ nm}))/ (673 \text{ nm} - 434 \text{ nm})$, however, the propagation of STDs was much simpler:

$$\text{STD}(R_{L2}^* - R_{L7}^*) = \left[(\text{STD}_{L2})^2 + (\text{STD}_{L7})^2 \right]^{1/2} \quad (3)$$

which produces the STDs that are small relative to the variations in 434 nm to 753 nm spectral slope (Figure 10c, corresponding L2 versus L7 histograms in Figures 4a–4g), and makes these variations to be statistically meaningful.

[41] Furthermore, compared to the even larger spectral slope variations from 434 nm to 673 nm (Figures 9b and 10d), the propagated STDs are even more insignificant, therefore further confirmed that the 434 nm to 673 nm spectral slope reduction following the increase of exposure time duration to be statistically meaningful.

[42] Similar to Figure 4, a set of seven L3 (673 nm) versus L7 (434 nm) 2-D filter histograms (not shown) has a similar temporal character; that is, the data points from the light-toned salty soils are separated into two data branches

in all seven 2-D histograms, while the degree of separation reduces in the 2-D histograms of later observations. When plotting the spectral slope(s) \pm STDOM, the error bars are even smaller (because each ROI contains >1000 pixels) than those in Figures 10c and 10d.

[43] Figure 10d further reveals that the decrease in the difference of 434 nm to 673 nm spectral slopes of two types of Tyrone salty soils is mainly caused by the spectral slope reduction of yellowish soils. This observation is consistent with the conclusion drawn based on the overall view from Figure 4 (and in Figure 28 by *Wang et al.* [2008]). On the basis of these results, a rough estimation on spectral slope change of yellowish Tyrone salty soils can be made, about 5% for 434 nm to 753 nm spectral slope; and about 7% for 434 nm to 673 nm spectral slope.

[44] The calculation of spectral slope can be affected by the general spectral albedo change caused by the changes in measurement time (local solar time, i.e., solar angle) and atmospheric conditions. The six periodic Tyrone observations (exclude the last one in sol 1062) used in our analysis were made from the exact same location (second winter campaign site, site 128 position 0), at almost same local solar time ($\Delta t_{\text{max}} \sim 61 \text{ min}$), with very similar solar azimuth angles ($\Delta \theta_{\text{max}} \sim 28.3^\circ$) and solar elevation angles ($\Delta \varphi_{\text{max}} \sim 14.8^\circ$), and relatively stable tau value. In addition, Figure 8 shows little to no variation in general spectral albedo of disturbed and nondisturbed basaltic soils. We believe that the use of the spectral slope calculation is a proper methodology to quantify the spectral variation of Tyrone yellowish salty soils.

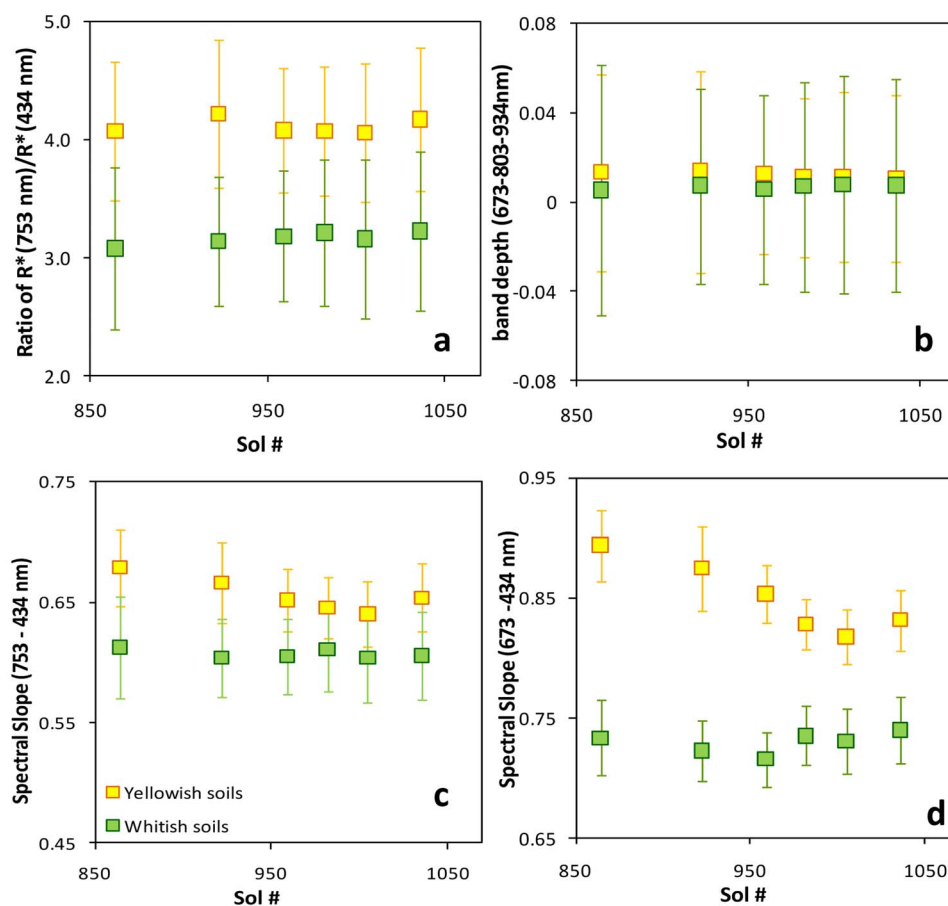


Figure 10. Quantification of the spectral variations among the six Pancam Tyrone monitoring observations. (a and b) The ratio of $R^*_{753\text{nm}}/R^*_{434\text{nm}}$ and the band depth at 803 nm between 673 and 934 nm. The plots demonstrate that extracting the variations of these two parameters from the spectra would be statistically meaningless. (c and d) The spectral slopes from 434 nm to 753 nm and from 434 nm to 673 nm. The plots demonstrate the variation of these spectral slope is statistically meaningful. The spectral slopes of yellowish salty soils (in both Figures 10c and 10d) were reduced, which caused the reduction of difference in spectral slopes between yellowish and whitish salty soils.

[45] The quantitative analysis (including STD propagations) based on the spectra extracted from selected ROIs are consistent with the overall view built on simply plotting the R^* values of all pixels of studied Pancam images (Figures 4a–4g), and also consistent with the conclusion of Wang *et al.* [2008], i.e., the reduction of separation of two data branches in L2 versus L7 2-D histograms being caused by the reduction of 434 nm to 753 nm spectral slope of yellowish salty soils.

2.2. Mineral Candidates for Tyrone Salty Soils

[46] Alpha-particle X-ray spectroscopy (APXS) and Mössbauer spectroscopy (MB) measurements were made on two Tyrone-offset targets: Tyrone–Berkner Island and Tyrone–Mount Darwin (about 11.6 m way from Tyrone site [Arvidson *et al.*, 2008]). Decorrelation Stretch (DCS) [e.g., Gillespie *et al.*, 1986] of Pancam images suggested these two targets to be the mixtures of Tyrone whitish salty soil with local basaltic soils [Wang *et al.*, 2008]. APXS data of these targets show a correlation of CaO versus SO_3 [Yen *et al.*, 2008], that implies Ca-sulfates being one of the

major components in Tyrone whitish salty soil. Mössbauer measurements of the same targets suggest 29% of total iron occur as ferric sulfates [Morris *et al.*, 2008] in those soils targeted by these two in situ instruments. The Tyrone yellowish salty soil was never measured by APXS and MB instruments. In addition, the hydrous nature of Tyrone salty soils were revealed by a series Mini-TES measurements, from both yellowish and whitish Tyrone soils [Wang *et al.*, 2008].

[47] The absorption band at ~ 803 nm in Pancam VIS-NIR spectra of Tyrone yellowish salty soils (Figure 2b) is suggestive of a similar feature seen in some ferric sulfates, and the average spectrum of Tyrone whitish salty soils (Figure 2b) exhibits similarities to spectra of some hydrated salts such as Fe-, Ca- Mg-sulfates and halides [Morris *et al.*, 2000; Lane *et al.*, 2008]. A Pancam-based spectral deconvolution study [Johnson *et al.*, 2007] provided additional first-order constraints on Fe-sulfates detections at Tyrone. They used a database of 84 laboratory spectra and a multiple end-member spectral mixing model to identify candidate Fe-sulfates and their assemblages that may contribute to the observed Pancam

spectra. They suggested that five ferric sulfates make up to 50% of typical Tyrone yellowish salty soil. Among the five, ferricopiapite $[\text{Fe}_{2/3}^{3+}\text{Fe}_4^{3+}(\text{SO}_4)_6(\text{OH})_2 \cdot 20(\text{H}_2\text{O})]$ was indicated to have the highest concentration (~27%). This analysis makes the basis for us to concentrate on the properties of ferricopiapite in following experimental investigation.

3. Experimental Investigations to Support Mission Data Analysis

[48] A laboratory experimental study of the fundamental properties of ferric sulfates bears an extreme importance for the interpretation of the mission observations, including the temporal spectral changes of ferric sulfates observed by the Spirit rover.

[49] Three groups of factors will determine the types of ferric sulfates present on the surface and within the subsurface of current Mars. First group is the formation conditions of ferric sulfates, including brine chemistry, temperature, the partial pressure of water, oxygen fugacity, and acidity of aqueous solution/droplet. Second group is the stability fields, phase boundaries, and the phase transition pathways of some ferric sulfates in $T, P_{\text{H}_2\text{O}}, \text{pH}, \text{Eh}$ (redox potential) space. The third group is the reaction rates of relevant processes under Mars past and present environment conditions. We have been conducting a set of systematic experiments to investigate those fundamental properties of a few important ferric sulfates to address these questions.

[50] Our experiments were conducted in three steps. At first, we synthesized eight ferric sulfates with different degrees of hydration, acidity, and crystallinity (ferricopiapite, paraconquimbite, kornelite, lausenite, pentahydrate, rhomboclase, mikasaite, and amorphous ferric-sulfate). Their identities were confirmed using XRD. Spectroscopic characterizations using Raman, MIR, NIR, and VIS-NIR were then conducted on all of them [Ling and Wang, 2010; Ling *et al.*, 2008, 2009]. Because of the importance of copiapite among common ferric sulfates, we synthesized its four chemical end-members: ferricopiapite, copiapite, magnesio-copiapite, and aluminocopiapite. Their identities were again confirmed using XRD, followed by spectroscopic characterizations [Kong *et al.*, 2009, 2011].

[51] We are now conducting the second step of this study, i.e., 150 experiments on the stability fields and phase transition pathways of five Fe-sulfates (the longest experiment lasted >25080 h) at three temperatures (50°C, 21°C, and 5°C) and ten levels of relative humidity (from 6% to 100% RH). The starting Fe-sulfates are ferricopiapite, rhomboclase, kornelite, pentahydrate, and an amorphous pentahydrated ferric sulfate. The fingerprint Raman spectra obtained in first step (e.g., Figure 12) were used for non-invasive phase identifications for the reaction products of intermediate stages during the second step. All Raman phase identifications are validated by gravimetric measurements of intermediate reaction products to monitor the change of water content [Wang *et al.*, 2010a].

[52] In section 3.1, we will present some results from above studies that have potential relevance to the Tyrone salty soil investigations. Especially those from ferricopiapite (based on the study of Johnson *et al.* [2007], which suggested ferricopiapite to be the major ferric sulfates in Tyrone yellowish salty soils), including its precipitation from

aqueous solution and its phase transition under different environment conditions. The complete results of the 150 experiments will be reported elsewhere.

3.1. Ferric Sulfates Precipitated From Fe-S-Bearing Aqueous Solution

[53] Our evaporation/precipitation experiments were started from an aqueous solution saturated with $\text{Fe}_2(\text{SO}_4)_3$ (from $\text{Fe}_2(\text{SO}_4)_3 \cdot 5\text{H}_2\text{O}$ of ACROS, code 345235000) at room temperature. The dark brown colored liquid was put into Petri dishes and placed at four temperature zones, 50°C, 21°C, 5°C and -10°C. At 21°C, the Petri dishes were placed in four desiccators containing saturated salt solutions as humidity buffers (KI, MgCl_2 , LiCl, and LiBr for RH ~ 73%, 34%, 11%, and 7%, based on the work of Greenspan [1977]), thus the evaporation/precipitation was conducted in controlled RH environments. The evaporation/precipitation at other temperatures (50°C in an oven, 5°C in a refrigerator and -10°C in a freezer) were conducted in open air, the corresponding RH values are in the range of <5%, 30%–46%, and 60%–74%, measured by a temperature/relative humidity sensing logger being placed in oven, in refrigerator, or in freezer for several days.

[54] Based on these experiments, we found that ferricopiapite $[\text{Fe}_{2/3}^{3+}\text{Fe}_4^{3+}(\text{SO}_4)_6(\text{OH})_2 \cdot 20(\text{H}_2\text{O})]$ is the most common ferric sulfate specie that precipitates from saturated $\text{Fe}^{3+}\text{-SO}_4^{2-}$ aqueous solutions under a quite wide temperature range (50°C to -10°C; Figures 11a and 11b) and a wide relative humidity range (RH > 11%). When adding extra H_2SO_4 into the starting solution, rhomboclase $[\text{Fe}(\text{H}_3\text{O})(\text{SO}_4)_2 \cdot 3\text{H}_2\text{O}]$ is the major precipitation product [Ling *et al.*, 2008]. In terrestrial field observations, ferricopiapite would precipitate from pH 1 to 0 solution, while rhomboclase from pH 0 to -2 [Nordstrom and Alpers, 1999]. Our experimental results are consistent with these observations.

[55] In the temperature range of our experiments (50°C to -10°C), we have not observed the direct precipitation of kornelite $[\text{Fe}_2(\text{SO}_4)_3 \cdot 7\text{H}_2\text{O}]$ and pentahydrate $[\text{Fe}_2(\text{SO}_4)_3 \cdot 5\text{H}_2\text{O}]$ from aqueous Fe-S-bearing solutions, although we did observe their deliquescence (normally through ferricopiapite) at various temperatures when RH is in the range of 60%–70%. When aqueous Fe-S solutions was placed under low relative humidity (<11%RH) at middle to high temperature (21°C and 50°C), amorphous ferric sulfates $[\text{Fe}_2(\text{SO}_4)_3 \cdot x\text{H}_2\text{O}]$ were observed (Figure 11d) to precipitate, which will be discussed later.

[56] In general, the precipitation of ferricopiapite (hydroxyl bearing) would drive down the pH level of residual solution thus would facilitate the precipitation of hydronium-bearing rhomboclase. However, in our experiments, these two species were never observed to coprecipitate. The precipitation product from the aqueous solution saturated with $\text{Fe}_2(\text{SO}_4)_3$ was always pure ferricopiapite. Rhomboclase only appears after many days of full solidification of ferricopiapite, at the extreme edge of “plate” (Figure 11c) or sharp spots of grain clusters (insert of Figure 11c) of ferricopiapite. Notice wherever residual solution still remains (shown in Figure 11b as a smooth surface of ferricopiapite, without visible fluid), no rhomboclase would appear. In addition, if the precipitated solid (ferricopiapite) was washed thoroughly with alcohol, no rhomboclase would appear later. We believe the reason for the delayed formation of rhomboclase is that the species

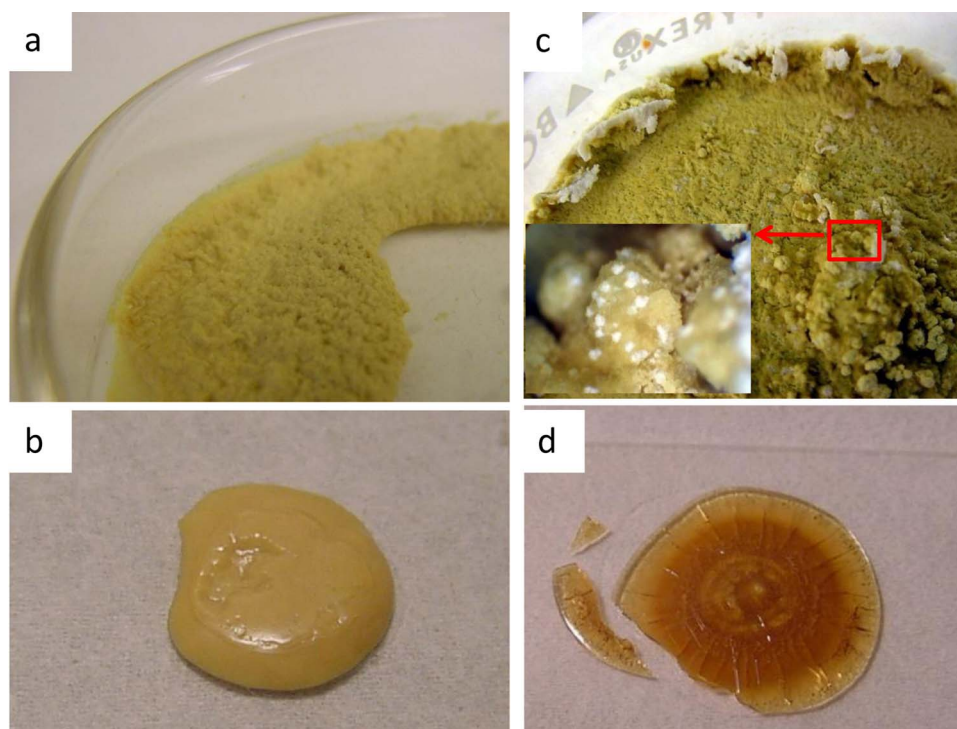
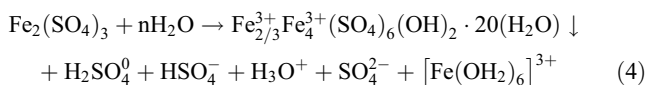
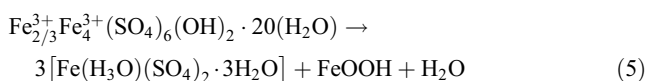


Figure 11. Ferric copiapite precipitated from aqueous solution saturated with Fe:SO₄ molar ratio equals 2:3 under different conditions: (a) at -10°C and 84% RH; (b) at 21°C and 73% RH; (c) at 5°C and 44% RH (the insert shows a zoom-in view of the area indicated by red rectangle); and (d) at 21°C and 11% RH, the precipitation is an amorphous ferric sulfate.

like H₂SO₄⁰, HSO₄⁻ exist in residual solution, which have reduced the concentration of H₃O⁺ (the higher concentration of total H₂SO₄ in solution, the higher H₂SO₄⁰ and HSO₄⁻ proportions).



Therefore, the delayed accumulation of H₃O⁺ in the residual solution has delayed the precipitation of rhomboclase. When the accumulation of H₃O⁺ reaches to certain level, the formation of rhomboclase can be stimulated. In addition, after the total solidification (as pure ferric copiapite) has been reached, the continuing dehydration will induce the conversion of ferric copiapite to rhomboclase (water/Fe ratio reduces from ~4.5 to 4), e.g.,



A total conversion of copiapites to rhomboclase was observed during a set of laboratory experiments, in which 19 copiapite samples with various degrees cation substitutions (by Mg²⁺, Fe²⁺, Fe³⁺, Al³⁺, Zn²⁺, Mn²⁺) were stored in 33% and 11% relative humidity buffers, respectively, at room temperature [Friedlander *et al.*, 2007]. After over 2 years' equilibrium processes, final phases of all samples were taken out and ten-spot Raman analyses were conducted on each sample. It was found that every copiapite sample was totally converted, mainly to rhomboclase, some to coquimbite and anhydrous ferric sulfates. Trace hematite was also observed.

Apparently, the conversion from copiapite type minerals (including variety of cation substitutions) to rhomboclase is a common process.

[57] Applying these laboratory observations to Tyrone salty soils, the suggestion made by Johnson *et al.* [2007] on the mineral candidates for Tyrone yellowish soil based on Pancam VIS-NIR spectral deconvolution, i.e., ferric copiapite (27%) and rhomboclase (3%) as the major phases, makes perfect sense if assuming they were direct precipitations from aqueous solutions (or droplets). In addition, the fact that ferric copiapite is observed to readily change to rhomboclase during dehydration is very important to understanding the temporal change of Tyrone yellowish soil. This chemical alteration (dehydration and change from hydroxyl bearing to hydronium bearing) was observed every time in the laboratory when holding the precipitated ferric copiapite directly (without alcohol washing) under low RH conditions at 5°C, 21°C, or even 50°C.

[58] Figure 12 shows the Raman (using a HoloLab5000-532 Raman system, made by Kaiser Optical Systems Inc.) and VIS-NIR spectra (using an Analytical Spectral Device, made by ASD Inc.) of rhomboclase and ferric copiapite. Raman spectra were used to make in situ identifications of these two species during above discussed experiments. In VIS-NIR spectral range, the most obvious differences in the spectrum of rhomboclase from that of ferric copiapite include a slightly higher albedo in blue (near 434 nm of Pancam L7 filter) and an absorption band near 778 nm (thus much lower albedo near 753 nm of Pancam L2 filter); therefore the spectral presentation of conversion from ferric copiapite to rhomboclase would be the reduction of Pancam spectral

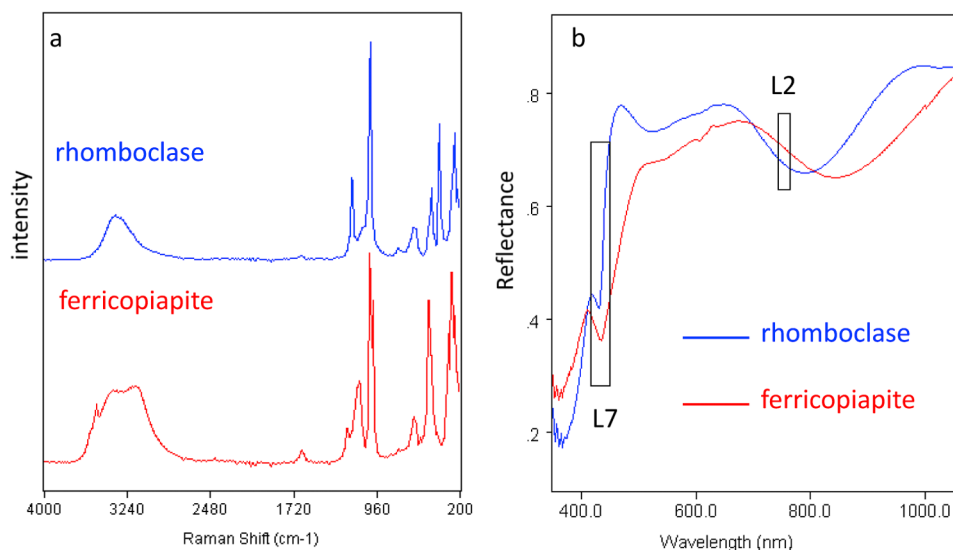


Figure 12. (a) Raman and (b) VIS-NIR spectra of ferricopiapite and rhomboclase. Positions and bandwidth of Pancam L2 (753 nm, $\Delta\lambda = 20$ nm) and L7 (432 nm, $\Delta\lambda = 32$ nm) filters [Bell *et al.*, 2003] are also presented in Figure 12b.

slope between L7 (434 nm) and L2 (753 nm), as observed from Tyrone yellowish salty soils after its 190 sol exposure to the current Mars surface atmospheric conditions.

3.2. Stability Field and Dehydration Pathways of Ferricopiapite

[59] Our experiments on the stability field and dehydration pathway of ferricopiapite were conducted in following way: about 100 mg synthetic ferricopiapite powder was put into a straight-wall glass reaction vial of 12 mm diameter. The noncapped reaction vial was put into a glass bottle of 25 mm diameter that is tightly sealed and contained saturated salt solution as RH buffers (ten RH buffers were used that cover a RH range from 6% to 100%). Thirty pairs of reaction vial/buffer bottle are placed in three temperature zones, $50 \pm 1^\circ\text{C}$ in an oven, $21 \pm 2^\circ\text{C}$ on lab bench, and $5 \pm 1^\circ\text{C}$ in a refrigerator, which ensured the hydration and dehydration of ferricopiapite being conducted in well-controlled T and RH zones. Gravimetric measurements were taken on the start, at several intermediate times, and on the final reaction products to evaluate the gain and the loss of water content. The phase identification of these ferric sulfates was made by noninvasive Raman spectroscopic measurements.

3.2.1. A Large Stability Field of Ferricopiapite at Low 5°C and -10°C

[60] The final ferric sulfate phases (after a maximum 24960 h of dehydration/rehydration process) from the 30 experiments started from ferricopiapite are shown in Figure 13. We can see that the deliquescence of ferricopiapite happens when $\text{RH} > 75\% - 80\%$ in a temperature range of 5 to 50°C . More importantly, within $11\% - 78\%$ RH at 5°C , ferricopiapite samples stay unchanged for almost 3 years with only one exception (section 3.3). At -10°C and $60\% < \text{RH} < 74\%$, ferricopiapite precipitated from aqueous solution (Figure 11a) has also stayed stable for almost 3 years (data points at -10°C in Figure 13). Note ferricopiapite has almost the highest hydration state (water/Fe ratio ~ 4.5) among the common

ferric sulfates, but it shows an extremely large stability field (down to 11% RH) at low temperature range.

3.2.2. Dehydration of Ferricopiapite

[61] Our experiments indicate that pure ferricopiapite has two pathways for dehydration. The first way is to form other crystalline ferric sulfates with lower hydration states (Figure 13), such as paracoquimbite [$\text{Fe}_2(\text{SO}_4)_3 \cdot 9\text{H}_2\text{O}$], kornelite and the pentahydrate, at middle to high temperature (after 437 days at 21°C , or after 9 days at 50°C). Relatively high temperature is required to provide activation energy for the changing of crystal structure from one to another.

[62] The 20 structural water molecules in a ferricopiapite formula unit (Figure 14a) take three types of crystallographic sites. The properties of these sites determine the ease of losing some H_2O during the dehydration of ferricopiapite. Among the 20 structural water, six H_2O surround a Fe^{3+} to form $[\text{Fe}(\text{OH}_2)_6]$ octahedra, eight H_2O are in two pairs of $[\text{Fe}(\text{OH}_2)_2(\text{OH})\text{O}_3]$ octahedra with each pair interconnected by sharing a common hydroxyl (OH), and six H_2O are not part of any S-centered tetrahedra or Fe-centered octahedra, but only linked to the framework by weak hydrogen bonding. In order to change this structure to, for example, a crystalline pentahydrate [Majzlan *et al.*, 2005], all hydrogen-bonded H_2O would be lost, Fe-centered octahedra would be reformed, i.e., $[\text{FeO}_3(\text{OH}_2)_3]$ and $[\text{FeO}_4(\text{OH}_2)_2]$, and all H_2O should be shared between octahedra and $[\text{SO}_4]$ tetrahedra (Figure 14b). The changes in the octahedral configuration and their connections to $[\text{SO}_4]$ would require certain activation energy, thus would normally happen at middle to high temperature range.

[63] Figure 15 shows Raman and VIS-NIR reflectance spectra taken from synthetic powder samples of paracoquimbite, kornelite, and pentahydrate in comparison with those of ferricopiapite. All three spectra of paracoquimbite, kornelite, and pentahydrate have much higher albedo near 432 nm (Pancam L7 filter) and absorption bands centered near 753 nm of Pancam L2 filter (~ 770 nm for paracoquimbite,

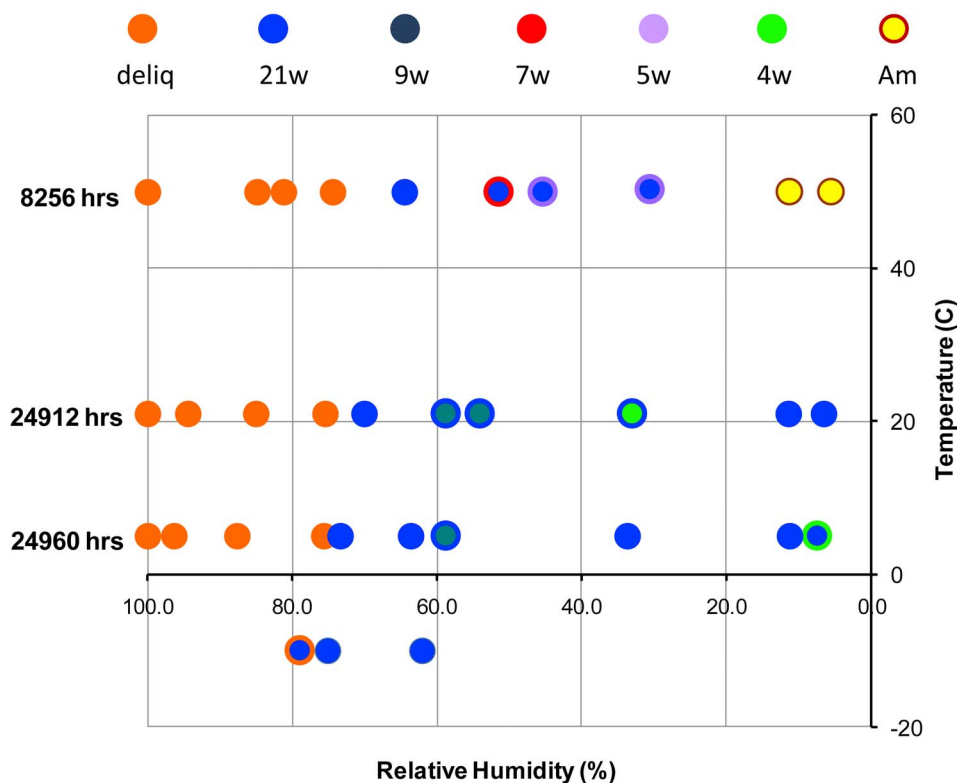


Figure 13. The final ferric sulfate phases from 30 hydration/dehydration experiments started from ferricopiapite at 5°C, 21°C, 50°C, and 10 relative humidity (RH) levels and from a few measurements at -10°C. The symbols of 21w, 9w, 7w, 5w, 4w, and Am represent ferricopiapite, paracoquimbite, kornelinite, pentahydrous ferric sulfate, and quasi-Am-I, identified by noninvasive Raman spectroscopic measurements.

~747 nm for kornelinite and ~720 nm for pentahydrate). Therefore the spectral presentation of a dehydration from ferricopiapite to paracoquimbite, kornelinite, or pentahydrate would be the reduction of spectral slope between L7 (434 nm) and L2 (753 nm), as observed from Tyrone yellowish salty soils.

[64] The second path of dehydration of ferricopiapite is to form amorphous (or quasi-amorphous) ferric sulfates, which started to appear after 20 h at 7%–11% RH and 50°C (Figure 13). In this case, the structural water molecules in ferricopiapite were pulled out by dehydration process, where there was not enough energy to modify the damaged ferricopiapite structure and to form a new crystalline phase, thus the dehydration produced an irregular structure.

3.2.3. Quasi-Amorphous Ferric Sulfates

[65] For ferric sulfates, we observed two types of amorphous or quasi-amorphous structures formed by two different ways. The first structure (quasi-amorphous ferric sulfates (quasi-Am-I)) was formed by fast dehydration of ferricopiapite. In order to better understand this amorphization process and the water holding capacity of the irregular structure, we conducted additional vacuum desiccation experiments in following way. About 50 mg ferricopiapite powder was put into each of 12 straight-wall uncapped glass vials of 12 mm diameter. Those vials were placed in a desiccator at room temperature. Under evacuation the desiccator can attain a vacuum with a pressure of 130 mtorr, corresponding a water vapor pressure of 0.09 Pa (calculated

from the laboratory T and RH of the day of experiment). This low water vapor pressure is in the range of water vapor pressure at the surface of Mars (with seasonal variation from 0.04 to 0.15 Pa [Smith *et al.*, 2004]). During this experiment, one sample vial was taken out from the desiccator at the following evacuation times: 5 min, 10 min, 20 min, 40 min, 60 min, 90 min, 120 min, and 17 h. The sample vial was immediately sealed and gravimetric and Raman measurements were made on the sample.

[66] Figure 16a shows the Raman spectra from several intermediate products of vacuum desiccation experiments. They demonstrated that after 5 min in vacuum, an obvious spectral pattern change (loss of peak details) happened, indicating a change in the structure of ferricopiapite. However, the modified spectral pattern (having two broad peaks mainly) stabilized between 1 h and 17 h evacuations; demonstrating that the loss of structural water had reached a limitation.

[67] Figure 16b shows the estimated loss of water per molecular formula of ferricopiapite based on gravimetric measurements. Because the high molar mass of ferricopiapite (1231.2), the loss of one water molecule per formula unit would only cause 1.5% of mass change (it would be 7% in epsomite $\text{MgSO}_4 \cdot 7\text{H}_2\text{O}$), thus using gravitational measurements to estimate the water loss in ferricopiapite has intrinsically a larger uncertainty than in Mg-sulfates. Nevertheless, Figure 16b demonstrates a trend of water loss in ferricopiapite during vacuum desiccation, and the maximum water loss reached in above experiment was six water molecules per

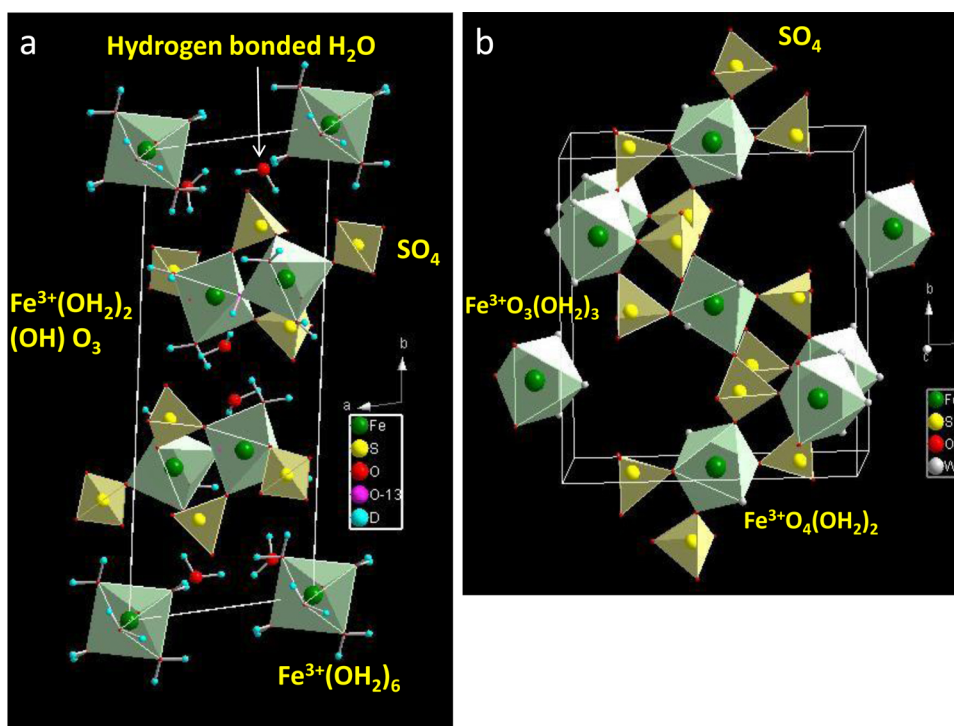


Figure 14. Crystal structures of (a) ferricopiapite $[\text{Fe}_{4.67}(\text{SO}_4)_6(\text{OH})_2 \cdot 20\text{H}_2\text{O}]$ and (b) pentahydrate $[\text{Fe}_2(\text{SO}_4)_3 \cdot 5\text{H}_2\text{O}]$. The different crystallographic sites of H_2O are shown.

formula unit of ferricopiapite. Based on ferricopiapite crystal structure (Figure 14a), we believe the water molecules that were lost during this vacuum desiccation experiment were the six hydrogen-bonded H_2O . The H_2O molecules as building block of $[\text{Fe}(\text{OH})_6]$ and $[\text{FeO}_3(\text{OH})(\text{OH}_2)_2]$ octahedra were not affected; that is, the major framework of ferricopiapite structure was kept, with distorted details due to the loss of six H_2O .

[68] The resulting ferric sulfate from this experiment held 14 to 19 structural water per $\text{Fe}_{4.67}(\text{SO}_4)_6(\text{OH})_2$. We demonstrated in the study of amorphous Mg-sulfates that the position of the Raman ν_1 peak (ν_1 peak of sulfates comes from the symmetric stretching mode of $[\text{SO}_4]^{2-}$ tetrahedron) shifts from 1016 to 1030 cm^{-1} following the decrease of water content per SO_4 from 3.2 to 2.0 [Wang *et al.*, 2009a]. The ferric sulfates with distorted structures produced in above

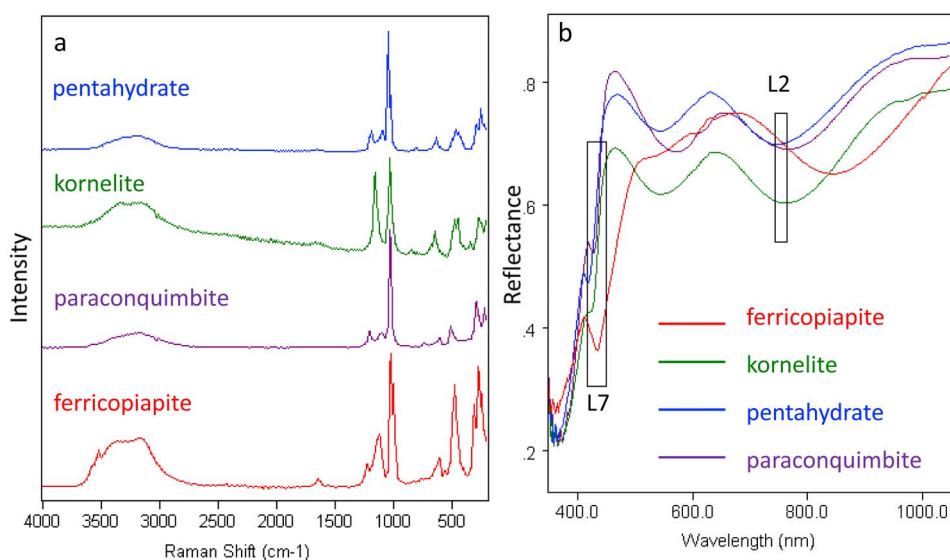


Figure 15. (a) Raman and (b) VIS-NIR spectra of paracoquimbite, kornelite, and pentahydrate compared with that of ferricopiapite. The positions and bandwidth of Pancam L2 and L7 filters are also presented.

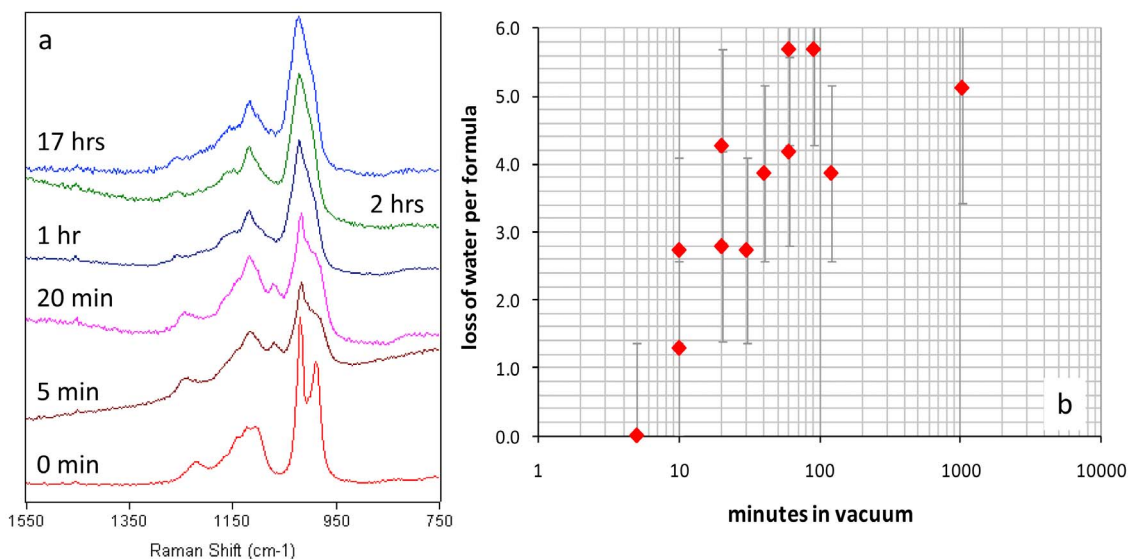


Figure 16. Results from a set of vacuum desiccation experiments. (a) The formation of quasi-amorphous ferric sulfate (quasi-Am-I) from ferricopiapite was demonstrated by the broadening of ν_1 peak and the loss of minor peaks in their Raman spectra. (b) The estimated loss of structural water molecules based on gravimetric measurements. Approximately six water molecules were lost at the end of desiccation experiment. The large error bars came from the fact that losing one water molecule in ferricopiapite will account for only 1.5% mass change and thus a very small variation in gravimetric measurements.

experiment have their ν_1 Raman peak shift from 1019 to 1023 cm^{-1} , only 4 cm^{-1} peak shift for a maximum loss of six structural waters. The weak influence of this H_2O loss on the Raman peak position is due to the weak hydrogen bonding of six H_2O to ferricopiapite structure, i.e., not being the major building block of framework. However, the obvious Raman spectral pattern change (Figure 16a) suggests a highly variable crystallographic environment surrounding each $[\text{SO}_4]$ tetrahedron, therefore a structural distortion had happened. Based on the similarity of its spectral pattern change to those during Mg-sulfate amorphization, we name this type of structure to be quasi-amorphous in following text; that is, quasi-Am-I. Further experimental study is continuing.

[69] The relative humidity in vacuum desiccator reached ~0%. This experiment is a logical extension from the dehydration experiments of ferricopiapite at low RH (7%–11%) and moderate temperature (50°C and 21°C; Figure 13). Both experiments demonstrate that amorphous structures with variable water content would be the ultimate product when ferricopiapite suddenly encounters an extra dry atmospheric condition at moderate temperature (21°C). At low temperature (5°C or -10°C), the low reaction rate can stimulate a competition between amorphization and straight dehydration to crystalline phases (observed for Mg-sulfates [Wang *et al.*, 2009a, 2009b, also submitted manuscript, 2010]). A similar set of experiments at low temperature will be conducted in our newly built Mars chamber to evaluate this possibility for ferric sulfates.

3.2.4. Amorphous Ferric Sulfates

[70] Amorphous ferric sulfates (Am-II) were found in the precipitation product (Figure 11d) from an aqueous ferric sulfate solution at low RH conditions (RH in 5%–11% range) and middle to high temperatures (21°C and 50°C).

They show a Raman spectral pattern (Figure 17) that bears some similarities with those of quasi-Am-I (Figure 16a), but having a much larger shift of peak position, i.e., from 1020 to 1035 cm^{-1} ($\Delta = 15 \text{ cm}^{-1}$) for ν_1 , and much wider peaks. The ν_1 peak position of amorphous sulfates has been found as an indication of their water content. For quasi-Am-I, the loss of six hydrogen-bounded water molecules in ferricopiapite structure only caused a shift of 4 cm^{-1} in ν_1 peak position. Therefore, the much large shift of ν_1 peak position of Am-II should therefore indicate a lower water content than the quasi-Am-I phase.

[71] We used a set of dehydration/rehydration experiments to evaluate the range of water content that can be held by this structure. An commercial amorphous ferric sulfate ($\text{Fe}_2(\text{SO}_4)_3 \cdot 5\text{H}_2\text{O}$, by ACROS, code 345235000) was used as the starting phase for 30 experiments at ten relative humidity levels and three temperatures. This amorphous ferric sulfate has a similar Raman spectral pattern as Am-II (Figure 17) with ν_1 peak position at 1034.3 cm^{-1} . During one experiment at 33.6% RH and 5°C, the amorphous ferric sulfate showed a slow increase of water content (based on gravimetric measurements), from five to eleven water molecules per $\text{Fe}_2(\text{SO}_4)_3$ formula, accompanied by a shift of Raman ν_1 peak position from 1035.1 cm^{-1} to 1020.2 cm^{-1} (Figure 18). After the ν_1 peak reached 1020 cm^{-1} , the continuation of rehydration caused the appearance of sharp crystalline Raman peaks of rhomboclase ($\text{FeH}(\text{SO}_4)_2 \cdot 4\text{H}_2\text{O}$), indicating that the sample has started recrystallization. Based on Figure 18, a rough estimation of water content in Am-II can be made using their Raman ν_1 peak positions, while the spectral pattern change (shown in Figure 16a) can serve as an indicator of the development of quasi-Am-I structure.

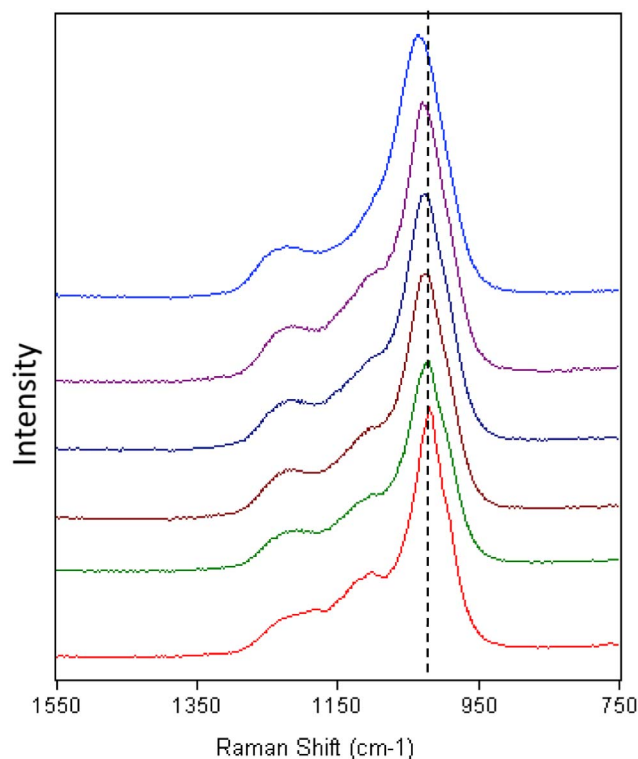


Figure 17. The ν_1 Raman peak position shifts (indicated by a vertical dash line) and the spectral pattern changes of Am-II phases, precipitated from aqueous solution at extra dry condition (RH < 11%).

3.2.5. XRD and VIS-NIR Spectra of Quasi-Am-I and Am-II

[72] Figure 19 shows the XRD patterns of quasi-Am-I and Am-II phases, compared to the XRD pattern of ferricopiapite. Obviously, Am-II has a total noncrystalline structure, while quasi-Am-I keeps certain similarities to the ferricopiapite structure (e.g., similar positions for two lines at 4.86 and 9.75, corresponding 010 and 020 faces). In addition, quasi-Am-I has a few very strong additional XRD lines (marked by asterisks in Figure 19), and shifted positions for many other minor lines.

[73] It is worth noting that although the XRD pattern of quasi-Am-I suggests a modified crystalline structure, its Raman spectral pattern suggests some highly irregular structural environments surrounding each $[\text{SO}_4]^{2-}$ tetrahedron, and gravimetric measurements suggest the loss of six structural water per ferricopiapite formula. The structural details of this phase and its relationship with Am-II are important topics for future study.

[74] Figure 20 shows the VIS-NIR reflectance spectra taken from quasi-Am-I and Am-II. A comparison with the spectrum of ferricopiapite indicates that quasi-Am-I has a generally reduced spectral contrast, which produces a higher albedo near 434 nm (Pancam L7 filter) and a shallow absorption band (although no change in band center ~ 920 nm from ferricopiapite) resulting in a lower albedo at 753 nm (Pancam L2 filter). The spectrum of Am-II has a slight higher albedo near 434 nm and an absorption band center near 760 nm resulting in a much lower albedo at 753 nm.

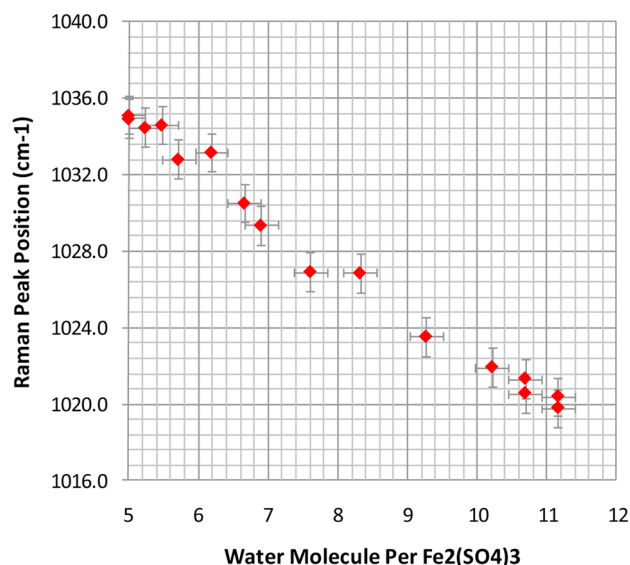


Figure 18. Changes in the Raman ν_1 peak position during rehydration of Am-II ($\text{Fe}_2(\text{SO}_4)_3 \cdot 5\text{H}_2\text{O}$) at 33.6% RH and 5°C. The position of ν_1 Raman peak shifts to lower wave number following the increase of water content per $\text{Fe}_2(\text{SO}_4)_3$, estimated from the results of gravimetric measurements.

Therefore, the transformation from ferricopiapite to quasi-Am-I or to Am-II will be expressed in VIS-NIR spectra by a reduction of Pancam spectral slope between L7 (434 nm) and L2 (753 nm), the same change as observed from Tyrone yellowish salty soils.

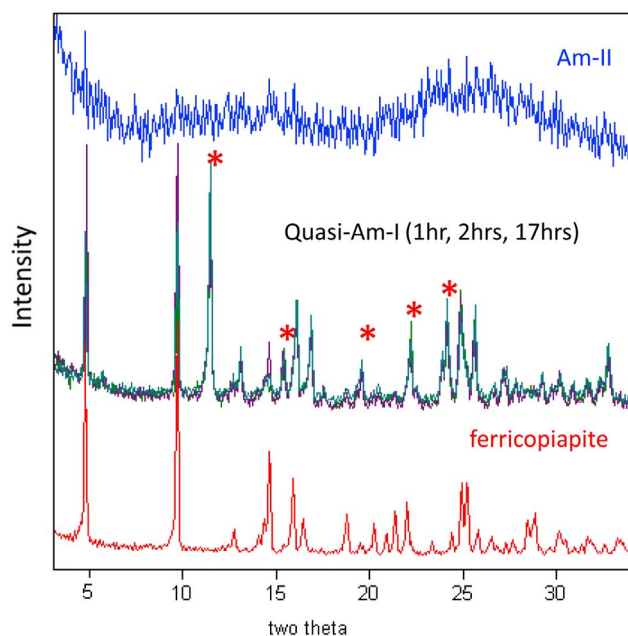


Figure 19. XRD patterns of quasi-Am-I (from 1 h, 2 h, and 17 h of vacuum desiccation), Am-II, and crystalline ferricopiapite. In the XRD patterns of quasi-Am-I (1 h, 2 h, 17 h), the additional XRD lines (compared with XRD lines of ferricopiapite) are marked by asterisks.

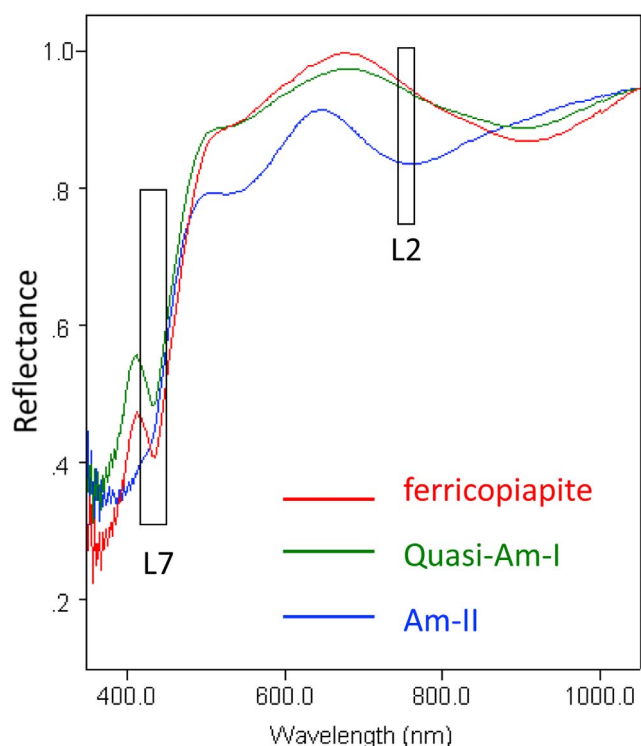


Figure 20. VIS-NIR spectra of quasi-Am-I, Am-II, and ferricopiapite. The positions and bandwidth of Pancam L2 and L7 filters are presented.

3.3. Three Potential Mechanisms

[75] Based on above experimental results, if we accept the major component of Tyrone yellowish salty soils is indeed ferricopiapite as indicated by *Johnson et al.* [2007], three dehydration mechanisms can be the potential causes to induce the reduction of Pancam spectral slope between L7 (434 nm) and L2 (753 nm) of Tyrone yellowish salty soils. They are: a combination of dehydration and chemical alteration of ferricopiapite to rhomboclase; the straight dehydration of ferricopiapite to paracoquimbite, kornelite, or pentahydrate; and the transformation to quasi-Am-I or Am-II.

[76] Comparing the reflectance spectra shown in Figures 12, 15, and 20 would suggest the amorphization of ferricopiapite to quasi-Am-I to be the most likely mechanism, since it produces a similar spectral pattern with reduced spectra contrast (i.e., reduction of absorption band depth at ~ 920 nm), while other processes produce band center blue shifts (to 720–780 nm). However, Tyrone yellowish salty soils are mixtures of many mineral species. The band center blue shift of one component may only induce a slight albedo reduction in the range of 673–753 nm, which would result as a decrease of spectral slope from 434 nm to 753 nm and the decrease of band depth centered at ~ 803 nm. Therefore, the conversions to rhomboclase, Am-II, paracoquimbite, kornelite, or pentahydrate as causes for temporal spectral change of Tyrone yellowish salty soil cannot be excluded based on reflectance spectral evidence.

[77] When considering the experimental conditions under which those dehydration processes occur, forming crystalline kornelite and pentahydrate from the dehydration of ferricopiapite is less favorable under current surface conditions at

Gusev, because a moderately high temperature (50°C in laboratory, that does not exist at the surface of Gusev) is needed to provide activation energy for the transformation from one crystalline structure to another. In addition, the partial conversion of ferricopiapite to paracoquimbite happened in our experiment after 437 days at 21°C and after 606 days at 5°C in a RH range of 54%–59%. We conclude that this conversion is unlikely to be the actual cause for the reduction of Pancam spectral slope, which happened in a shorter time period and in a much dry environment.

[78] In contrast, amorphization can happen. We have demonstrated that when exposing ferricopiapite suddenly to a near-vacuum environment with extremely low water vapor pressure $P_{\text{H}_2\text{O}}$ in laboratory, the hydrogen-bounded structural water molecules in ferricopiapite are readily lost forming quasi-Am-I type of ferric sulfate (s) with 14–19 structural H_2O per ferricopiapite molecule. In our experiments, after 17 h at $P \sim 130$ mtorr, $P_{\text{H}_2\text{O}} \sim 0.09$ Pa, and 21°C, we were not able to form Am-II type of amorphous ferric sulfate (s) (with 5–11 structural H_2O). Nevertheless, the possibility of further pulling out H_2O from ferricopiapite structure during a much longer period (e.g., 278 sols for Tyrone soils) cannot be ruled out.

[79] In addition, when excavating ferricopiapite from the subsurface and exposing it to an extra dry environment, the dehydration plus chemical alteration to form rhomboclase can readily happen, as demonstrated by our laboratory experiments at various temperatures. The only condition for this process NOT to occur in the laboratory is to wash the previously precipitated ferricopiapite thoroughly with 95% alcohol which removes almost all remain H_3O^+ ions (no applicable for Tyrone salty soils).

[80] Table 1 lists the spectral slopes from 753 nm to 434 nm in the laboratory VIS-NIR spectra obtained from synthetic ferricopiapite, quasi-Am-I, Am-II, and rhomboclase. These slopes were calculated using the reflectance values averaged over 20 nm bandwidth centered at 753 nm (to match the bandwidth of Pancam L2 filter) and over 32 nm bandwidth centered at 434 nm (to match the bandwidth of Pancam L7 filter). These calculated spectral slope variations can thus be used to compare with those from Pancam Tyrone observations. Note that even the transformation of ferricopiapite to quasi-Am-I with the smallest spectral slope change (17%) is large enough to produce the $<10\%$ spectral slope changes observed in Tyrone yellowish soils. Therefore it is possible that both amorphization and chemical alteration of ferricopiapite can possibly occur within Tyrone

Table 1. The Spectral Slopes Between 434 nm and 753 nm of Four Synthetic Ferric Sulfates and the Reduction in Spectral Slope When Comparing the Spectral Slope Value of Ferricopiapite With Others

	753–434 nm SS ^a	Reduction of SS From Ferricopiapite
Ferricopiapite	1.5942	
Quasi-Am-I (17 h)	1.3291	17%
Am-II	1.1990	25%
Rhomboclase	0.8301	48%

^aThe spectral slopes (SS) were calculated using the reflectance values averaged over the bandwidths of Pancam L2 and L7 filters.

yellowish soils, and to produce the temporal VIS-NIR spectral variations.

4. Significance

[81] The significance of finding temporal spectral change of Tyrone yellowish soil is that it indicates the subsurface salty soils were originally NOT in equilibrium with the atmospheric conditions at the surface of Gusev region. In other words, there is a relative humidity gradient in the upper few tens of centimeters depth below the surface in the Tyrone area.

[82] There are two factors that influence the relative humidity (RH) of a local environment on Mars. Globally, the RH at the surface of Mars is determined by near surface temperature and the water vapor partial pressure. Locally and especially at certain depth of subsurface enriched with hydrous salts (and/or ground ice), e.g., where the yellowish soils may have originated, RH would be mostly buffered by the hydrous salts (and/or ice) buried at that level and deeper, and would be much less influenced by the surface atmospheric conditions. Our measurements indicate that hydrous sulfates are all good RH buffers. A sealed bottle filled with ferricopiapite at -10°C can maintain a RH range of 75%–79%, and a sealed bottle filled with $\text{MgSO}_4 \cdot 7\text{H}_2\text{O}$ at -10°C can maintain a RH range of 96%–97%.

[83] The second factor that influences the relative humidity (RH) at subsurface is the average temperature and the range of temperature variation. Thermal model calculations [Paige, 1992; Mellon *et al.*, 2004; Bandfield, 2007] suggest for a two-layer regolith, made of a layer of high thermal inertia material covered by a layer of low thermal inertia materials (e.g., ordinary surface dust on Mars), a very different temperature profile would occur in the subsurface, when compared with that of an one-layer homogeneous regolith. In the work by Mellon *et al.* [2004] two-layer regolith modeling, ground ice has a much higher thermal inertia ($2290 \text{ J m}^{-2} \text{ K}^{-1} \text{ s}^{-1/2}$) than that of surface dust ($200\text{--}250 \text{ J m}^{-2} \text{ K}^{-1} \text{ s}^{-1/2}$, by Ferguson *et al.* [2006]), a lower average temperature and smaller temperature oscillation (than T and ΔT at surface) would occur within subsurface which would help the preservation of ground ice.

[84] At Tyrone area (Gusev), it is reasonable to assume that the hydrous sulfates have a higher thermal inertia than that of ordinary surface dust. Thus within a sulfates-enriched regolith layer covered by a layer of ordinary surface dust, a similarly colder average temperature and a smaller magnitude of temperature oscillation would occur during Mars diurnal and seasonal cycles (based on the model of Mellon *et al.* [2004]); that is, the influence of atmospheric temperature variations were partially (or totally, at deeper depth) blocked. Therefore without considering the RH buffer effects of hydrous salts, the special temperature profile in sulfates-enriched regolith layer itself would produce a relatively higher average RH value and a smaller RH variation range (than those at surface), which will further help to maintain the stability of hydrated sulfates. Examples include ferricopiapite (at -10°C ; Figure 13), epsomite [Wang *et al.*, 2009b], and gypsum [Vaniman *et al.*, 2009].

[85] During the high obliquity period, or during the winter time and the early morning hours of moderate obliquity period, it would be quite possible that the zone temperature

drops to below the local frost point temperature, and the net condensation of water vapor in interstitial space among mineral grains happens (i.e., ice forming), which means a $\text{RH} \sim 100\%$. Under that condition, meridianiite ($\text{MgSO}_4 \cdot 11\text{H}_2\text{O}$) and various highly hydrous ferric sulfates can form and survive.

[86] In other words, the subsurface salty soils, if they are enriched with hydrous salts (with large quantity and depth), can build a favorable subsurface environment with right T-RH conditions to maintain the hydrous species with the highest degrees of hydration. These subsurface hydrous salts can be the source for high values of water-equivalent hydrogen detected at two large equatorial regions on Mars by the Neutron Spectrometer on Mars Odyssey Orbiter [Feldman *et al.*, 2004; Wang *et al.*, 2010b].

[87] **Acknowledgments.** We thank NASA for funding the MER Athena Science team and the JPL engineering team for continuing to successfully operate the Mars Exploration Rovers. We thank the support from Pancam team, Jim Bell, Jonathan Joseph, Jeffery Johnson, and Melissa Rice, for providing upgraded MERTOOLS that increase the data analysis capability and for excellent suggestions in Pancam data analysis. We thank our colleagues at Washington University in St. Louis, Raymond Arvidson, John Freeman, and Bradley Jolliff, for supporting our laboratory experiments. The experimental investigation was funded by NASA Mars Fundamental Research Program NNX07AQ34G, with supplementary support from the McDonnell Center for Space Sciences at Washington University. Z. C. Ling was funded by a special fund from Shandong University for his study at Washington University in St. Louis. Additionally, we thank Vincent F. Chevrier and the editor of this manuscript for providing two sets of excellent criticisms and suggestions, which helped us to improve the quality of data analysis and the manuscript.

References

- Arvidson, R. E., F. Poulet, J.-P. Bibring, M. Wolff, A. Gendrin, R. V. Morris, J. J. Freeman, Y. Langevin, N. Mangold, and G. Bellucci (2005), Spectral reflectance and morphologic correlations in eastern Terra Meridiani, Mars, *Science*, *307*, 1591–1594, doi:10.1126/science.1109509.
- Arvidson, R. E., et al. (2008), Spirit Mars Rover Mission to the Columbia Hills, Gusev crater: Mission overview and selected results from the Cumberland Ridge to Home Plate, *J. Geophys. Res.*, *113*, E12S33, doi:10.1029/2008JE003183.
- Arvidson, R. E., et al. (2010), Spirit Mars Rover Mission: Overview and selected results from the northern Home Plate Winter Haven to the side of Scamander crater, *J. Geophys. Res.*, *115*, E00F03, doi:10.1029/2010JE003633.
- Bandfield, J. L. (2007), High-resolution subsurface water-ice distribution on Mars, *Nature*, *447*, 64–67, doi:10.1038/nature05781.
- Bell, J. F., et al. (2003), Mars Exploration Rover Athena Panoramic Camera (Pancam) investigation, *J. Geophys. Res.*, *108*(E12), 8063, doi:10.1029/2003JE002070.
- Bell, J. F., III, J. Joseph, J. N. Sohl-Dickstein, H. M. Arneson, M. J. Johnson, M. T. Lemmon, and D. Savransky (2006), In-flight calibration and performance of the Mars Exploration Rover Panoramic Camera (Pancam) instruments, *J. Geophys. Res.*, *111*, E02S03, doi:10.1029/2005JE002444.
- Bibring, J. P., et al. (2005), Mars surface diversity as observed by the OMEGA/Mars Express investigation, *Science*, *307*, 1576–1581, doi:10.1126/science.1108806.
- Bishop, J. L., et al. (2008), Phyllosilicate diversity and past aqueous activity revealed at Mawrth Vallis, Mars, *Science*, *321*, 830–833, doi:10.1126/science.1159699.
- Chevrier, V. F., and T. S. Altheide (2008), Low temperature aqueous ferric sulfate solutions on the surface of Mars, *Geophys. Res. Lett.*, *35*, L22101, doi:10.1029/2008GL035489.
- Chipera, S. J., and D. T. Vaniman (2007), Experimental stability of magnesium sulfate hydrates that may be present on Mars, *Geochim. Cosmochim. Acta*, *71*(1), 241–250, doi:10.1016/j.gca.2006.07.044.
- Chou, I.-M., and R. R. Seal II (2007), Magnesium and calcium sulfate stabilities and the water budget of Mars, *J. Geophys. Res.*, *112*, E11004, doi:10.1029/2007JE002898.
- Ehlmann, B. L., J. F. Mustard, C. I. Fassett, S. C. Schon, J. W. Head III, D. J. Des Marais, J. A. Grant, and S. L. Murchie (2008a), Clay minerals in delta deposits and organic preservation potential on Mars, *Nat. Geosci.*, *1*, 355–358, doi:10.1038/ngeo207.

- Ehlmann, B. L., et al. (2008b), Orbital identification of carbonate-bearing rocks on Mars, *Science*, 322, 1828–1832, doi:10.1126/science.1164759.
- Feldman, W. C., et al. (2004), The global distribution of near-surface hydrogen on Mars, *J. Geophys. Res.*, 109, E09006, doi:10.1029/2003JE002160.
- Ferguson, R. L., P. R. Christensen, J. F. Bell III, M. P. Golombek, K. E. Herkenhoff, and H. H. Kieffer (2006), Physical properties of the Mars Exploration Rover landing sites as inferred from Mini-TES-derived thermal inertia, *J. Geophys. Res.*, 111, E02S21, doi:10.1029/2005JE002583.
- Friedlander, L. R., N. J. Tosca, and R. E. Arvidson (2007), Preliminary experiments in the systematic investigation of the spectroscopic properties of synthetic copiapite group minerals, *Lunar Planet. Sci. [CD-ROM]*, XXXVIII, abstract 2049.
- Gendrin, A., et al. (2005), Sulfates in Martian layered terrains: The OMEGA/Mars Express view, *Science*, 307, 1587–1591, doi:10.1126/science.1109087.
- Gillespie, A., A. B. Kahle, and R. E. Walker (1986), Color enhancement of highly correlated images. I. Decorrelation and HIS contrast enhancement, *Remote Sens. Environ.*, 20, 209–235, doi:10.1016/0034-4257(86)90044-1.
- Greenspan, L. (1977), Humidity fixed points of binary saturated aqueous solutions, *J. Res. Natl. Bur. Stand., Sect. A*, 81A, 89–96.
- Haskin, L. A., et al. (2005), Water alteration of rocks and soils from the Spirit Rover site, Gusev crater, Mars, *Nature*, 436, 66–69, doi:10.1038/nature03640.
- Johnson, J. R., J. F. Bell III, E. Cloutis, M. Staid, W. H. Farrand, T. McCoy, R. Rice, A. Wang, and A. Yen (2007), Mineralogic constraints on sulfur-rich soils from Pancam spectra at Gusev crater, Mars, *Geophys. Res. Lett.*, 34, L13202, doi:10.1029/2007GL029894.
- Klingelhöfer, G., et al. (2004), Jarosite and hematite at Meridiani Planum from Opportunity's Mössbauer spectrometer, *Science*, 306, 1740–1745, doi:10.1126/science.1104653.
- Kong, W. G., A. Wang, J. J. Freeman, and P. S. Sobron (2009), A comprehensive spectroscopic study (Raman, MIR, Vis-NIR, LIBS, XRD) of synthetic Fe^{2+} , Fe^{3+} , Mg^{2+} , Al^{3+} copiapites, *Lunar Planet. Sci. [CD-ROM]*, XXXX, abstract 1649.
- Kong, W. G., A. Wang, J. J. Freeman, and P. S. Sobron (2011), A comprehensive spectroscopic study of synthetic Fe^{2+} , Fe^{3+} , Mg^{2+} , and Al^{3+} copiapite by Raman, XRD, LIBS, MIR and VIS-NIR, *J. Raman Spectrosc.*, doi:10.1002/jrs.2790, in press.
- Lane, M. D., J. L. Bishop, M. D. Dyar, P. L. King, M. Parente, and B. C. Hyde (2008), Mineralogy of the Paso Robles soils on Mars, *Am. Mineral.*, 93, 728–739, doi:10.2138/am.2008.2757.
- Langevin, Y., F. Poulet, J.-P. Bibring, and B. Gondet (2005), Sulfates in the north polar region of Mars detected by OMEGA/Mars Express, *Science*, 307, 1584–1586, doi:10.1126/science.1109091.
- Lewis, K. W., O. Aharonson, J. P. Grotzinger, S. W. Squyres, J. F. Bell III, L. S. Crumpler, and M. E. Schmidt (2008), Structure and stratigraphy of Home Plate from the Spirit Mars Exploration Rover, *J. Geophys. Res.*, 113, E12S36, doi:10.1029/2007JE003025.
- Lichtenberg, K. A., et al. (2009), Stratigraphy and relationship of hydrated minerals in the layered deposits of Aram Chaos, Mars, *Lunar Planet. Sci. [CD-ROM]*, XXXX, abstract 2326.
- Lichtenberg, K. A., et al. (2010), Stratigraphy of hydrated sulfates in the sedimentary deposits of Aram Chaos, Mars, *J. Geophys. Res.*, 115, E00D17, doi:10.1029/2009JE003353.
- Ling, Z. C., and A. Wang (2010), A systematic spectroscopic study of eight hydrous ferric sulfates relevant to Mars, *Icarus*, 209, 422–433, doi:10.1016/j.icarus.2010.05.009.
- Ling, Z. C., A. Wang, B. L. Jolliff, R. E. Arvidson, and H. R. Xia (2008), A new phase of hydrated ferric sulfates, lausenite?, paper presented at 8th International Conference on Raman Spectroscopy Applied to Earth Science, Int. GeoRaman Conf. Coord. Comm., Ghent, Belgium.
- Ling, Z. C., A. Wang, and C. Li (2009), Comparative spectroscopic study of three ferric sulfates: Kornelinite, lausenite and pentahydrate, *Lunar Planet. Sci. [CD-ROM]*, XXXX, abstract 1867.
- Majzlan, J., C. Botez, and P. W. Stephens (2005), The crystal structures of synthetic $\text{Fe}_2(\text{SO}_4)_3(\text{H}_2\text{O})_5$ and the type specimen of lausenite, *Am. Mineral.*, 90, 411–416, doi:10.2138/am.2005.1701.
- McLennan, S., R. E. Arvidson, B. C. Clark, M. P. Golombek, J. P. Grotzinger, B. L. Jolliff, A. H. Knoll, S. W. Squyres, N. J. Tosca, and the Athena Science Team (2007), Geochemistry, mineralogy and diagenesis of the Burns Formation at Meridiani Planum: Insights into the sedimentary rock cycle on Mars, in *Seventeenth International Conference on Mars, July 9–13, 2007, Pasadena CA [CD-ROM]*, LPI Contrib., 1353, abstract 3231.
- McSween, H. Y., et al. (2004), Basaltic rocks analyzed by the Spirit Rover in Gusev crater, *Science*, 305, 842–845, doi:10.1126/science.3050842.
- McSween, H. Y., et al. (2006), Characterization and petrologic interpretation of olivine-rich basalts at Gusev crater, Mars, *J. Geophys. Res.*, 111, E02S10, doi:10.1029/2005JE002477.
- McSween, H. Y., et al. (2008), Mineralogy of volcanic rocks in Gusev crater, Mars: Reconciling Mössbauer, Alpha Particle X-Ray Spectrometer, and Miniature Thermal Emission Spectrometer spectra, *J. Geophys. Res.*, 113, E06S04, doi:10.1029/2007JE002970.
- Mellon, M. T., W. C. Feldman, and T. H. Prettyman (2004), The presence and stability of ground ice in the southern hemisphere of Mars, *Icarus*, 169, 324–340, doi:10.1016/j.icarus.2003.10.022.
- Milliken, R. E., J. Grotzinger, J. Grant, S. Murchie, and the CRISM Science Team (2007a), Clay minerals in Holden crater as observed by MRO CRISM, in *Seventeenth International Conference on Mars, July 9–13, 2007, Pasadena CA [CD-ROM]*, LPI Contrib., 1353, abstract 3282.
- Milliken, R. E., J. Grotzinger, R. A. Beyer, S. Murchie, A. McEwen, and the CRISM Science Team (2007b), Evidence for salt tectonics in Valles Marineris, Mars, in *Seventeenth International Conference on Mars, July 9–13, 2007, Pasadena CA [CD-ROM]*, LPI Contrib., 1353, abstract 3383.
- Milliken, R. E., et al. (2008), Spectral evidence for sedimentary silica on Mars, *Lunar Planet. Sci. [CD-ROM]*, XXXIX, abstract 2025.
- Milliken, R. E., K. S. Edgett, G. Swayze, R. N. Clark, B. J. Thomson, R. Anderson, and J. F. Bell III (2009), Clay and sulfate-bearing rocks in a stratigraphic sequence in Gale crater, *Lunar Planet. Sci. [CD-ROM]*, XXXX, abstract 1479.
- Ming, D. W., et al. (2008), Geochemical properties of rocks and soils in Gusev crater, Mars: Results of the Alpha Particle X-Ray Spectrometer from Cumberland Ridge to Home Plate, *J. Geophys. Res.*, 113, E12S39, doi:10.1029/2008JE003195.
- Morris, R. V., et al. (2000), Mineralogy, composition, and alteration of Mars Pathfinder rocks and soils: Evidence from multispectral, elemental, and magnetic data on terrestrial analogue, SNC meteorite, and Pathfinder samples, *J. Geophys. Res.*, 105, 1757–1817, doi:10.1029/1999JE001059.
- Morris, R. V., et al. (2006), Mössbauer mineralogy of rock, soil, and dust at Gusev crater, Mars: Spirit's journey through weakly altered olivine basalt on the plains and pervasively altered basalt in the Columbia Hills, *J. Geophys. Res.*, 111, E02S13, doi:10.1029/2005JE002584.
- Morris, R. V., et al. (2008), Iron mineralogy and aqueous alteration from Husband Hill through Home Plate at Gusev crater, Mars: Results from the Mössbauer instrument on the Spirit Mars Exploration Rover, *J. Geophys. Res.*, 113, E12S42, doi:10.1029/2008JE003201.
- Murchie, S., et al. (2007), CRISM mapping of layered deposits in western Candor Chasma, in *Seventeenth International Conference on Mars, July 9–13, 2007, Pasadena CA [CD-ROM]*, LPI Contrib., 1353, abstract 3238.
- Mustard, J. F., S. L. Murchie, S. M. Pelkey, B. L. Ehlmann, R. E. Milliken, J. A. Grant, J.-P. Bibring, F. Poulet, J. Bishop, and E. Noe Dobrea (2008), Hydrated silicate minerals on Mars observed by the Mars Reconnaissance Orbiter CRISM instrument, *Nature*, 454, 305–309, doi:10.1038/nature07097.
- Nordstrom, D. K., and C. N. Alpers (1999), Negative pH, efflorescent mineralogy, and consequences for environmental restoration at the Iron Mountain Superfund site, California, *Proc. Natl. Acad. Sci. U. S. A.*, 96, 3455–3462, doi:10.1073/pnas.96.7.3455.
- Paige, D. A. (1992), The thermal stability of near surface ground ice on Mars, *Nature*, 356, 43–45, doi:10.1038/356043a0.
- Reid, R. J., et al. (1999), Imager for Mars Pathfinder (IMP) image calibration, *J. Geophys. Res.*, 104, 8907–8925, doi:10.1029/1998JE000111.
- Rice, M. S., J. F. Bell III, A. Wang, and E. A. Cloutis (2008), Vis-NIR spectral characterization of Si-rich deposits at Gusev crater, Mars, *Lunar Planet. Sci. [CD-ROM]*, XXXIX, abstract 2138.
- Rice, M. S., J. F. Bell III, E. A. Cloutis, A. Wang, S. W. Ruff, M. A. Craig, D. T. Bailey, J. R. Johnson, P. A. de Souza Jr., and W. H. Farrand (2009), Silica-rich deposits and hydrated minerals at Gusev crater, Mars: Vis-NIR spectral characterization and regional mapping, *Icarus*, 205, 375–395, doi:10.1016/j.icarus.2009.03.035.
- Rice, M. S., J. F. Bell III, E. A. Cloutis, J. J. Wray, K. E. Herkenhoff, R. Sullivan, J. R. Johnson, and R. B. Anderson (2011), Temporal observations of bright soil exposures at Gusev crater, *J. Geophys. Res.*, 116, E00F14, doi:10.1029/2010JE003683.
- Roach, L. H., J. F. Mustard, S. L. Murchie, J. L. Bishop, C. M. Weitz, A. T. Knudson, J.-P. Bibring, S. M. Pelkey, B. L. Ehlmann, and the CRISM Science Team (2007), Magnesium and iron sulfate variety and distribution in East Candor and Capri Chasma, Valles Marineris, in *Seventeenth International Conference on Mars, July 9–13, 2007, Pasadena CA [CD-ROM]*, LPI Contrib., 1353, abstract 3223.
- Roach, L. H., J. F. Mustard, S. L. Murchie, J.-P. Bibring, R. E. Arvidson, J. L. Bishop, R. E. Milliken, F. P. Seelos, and the CRISM Science Team (2008), Constraints on the rate of sulfate phase changes in Valles Marineris interior layered deposits, *Lunar Planet. Sci. [CD-ROM]*, XXXIX, abstract 1823.
- Roach, L. H., J. F. Mustard, S. L. Murchie, J.-P. Bibring, F. Forget, K. W. Lewis, O. Aharonson, M. Vincendon, and J. L. Bishop (2009a), Testing

- evidence of recent hydration state change in sulfates on Mars, *J. Geophys. Res.*, *114*, E00D02, doi:10.1029/2008JE003245.
- Roach, L. H., J. F. Mustard, S. L. Murchie, J. L. Bishop, B. L. Ehlmann, K. Lichtenberg, M. Parente, and the CRISM Science Team (2009b), Sulfate and hematite stratigraphy in Capri Chasma, Valles Marineris, *Lunar Planet. Sci.* [CD-ROM], XXXX, abstract 1826.
- Roach, L. H., F. Mustard, S. L. Murchie, J. L. Bishop, B. L. Ehlmann, R. E. Milliken, K. Lichtenberg, and M. Parente (2009c), Hydrated mineral stratigraphy in Ius Chasma, Valles Marineris, *Lunar Planet. Sci.* [CD-ROM], XXXX, abstract 1834.
- Schmidt, M. E., et al. (2008), Hydrothermal origin of halogens at Home Plate, Gusev crater, *J. Geophys. Res.*, *113*, E06S12, doi:10.1029/2007JE003027.
- Smith, M. D., et al. (2004), First atmospheric science results from the Mars Exploration Rovers Mini-TES, *Science*, *306*, 1750–1753, doi:10.1126/science.1104257.
- Sohl-Dickstein, J., J. R. Johnson, W. M. Grundy, E. A. Guinness, T. Graff, M. K. Shepard, R. E. Arvidson, J. F. Bell III, P. R. Christensen, and R. V. Morris (2005), Modeling visible/near-infrared photometric properties of dustfall on a known substrate, *Lunar Planet. Sci.* [CD-ROM], XXXVI, abstract 2235.
- Squyres, S. W., et al. (2008), Detection of silica-rich deposits on Mars, *Science*, *320*, 1063–1067, doi:10.1126/science.1155429.
- Tosca, N. S., S. M. McLennan, D. Lindsley, and M. A. A. Schoonen (2004), Acid-sulfate weathering of synthetic Martian basalt: The acid fog model revisited, *J. Geophys. Res.*, *109*, E05003, doi:10.1029/2003JE002218.
- Vaniman, D. T., and S. J. Chipera (2006), Transformation of Mg- and Ca-sulfate hydrates in Mars regolith, *Am. Mineral.*, *91*, 1628–1642.
- Vaniman, D. T., D. L. Bish, S. J. Chipera, C. I. Fialips, J. W. Carey, and W. C. Feldman (2004), Magnesium sulphate salts and the history of water on Mars, *Nature*, *431*, 663–665, doi:10.1038/nature02973.
- Vaniman, D. T., D. L. Bish, and S. J. Chipera (2009), Bassanite on Mars, *Lunar Planet. Sci.* [CD-ROM], XXXX, abstract 1654.
- Wang, A., and J. J. Freeman (2009), Pathways and rates of Mg-sulfate dehydration and rehydration on Mars, *Lunar Planet. Sci.*, [CD-ROM], XL, abstract 2029.
- Wang, A., et al. (2006a), Sulfate deposition in subsurface regolith in Gusev crater, Mars, *J. Geophys. Res.*, *111*, E02S17, doi:10.1029/2005JE002513.
- Wang, A., et al. (2006b), Evidence of phyllosilicates in Woolly Patch, an altered rock encountered at West Spur, Columbia Hills, by the Spirit Rover in Gusev crater, Mars, *J. Geophys. Res.*, *111*, E02S16, doi:10.1029/2005JE002516.
- Wang, A., et al. (2008), Light-toned salty soils and coexisting Si-rich species discovered by the Mars Exploration Rover Spirit in Columbia Hills, *J. Geophys. Res.*, *113*, E12S40, doi:10.1029/2008JE003126.
- Wang, A., J. J. Freeman, and B. L. Jolliff (2009), Phase transition pathways of the hydrates of magnesium sulfate in the temperature range 50°C to 5°C: Implication for sulfates on Mars, *J. Geophys. Res.*, *114*, E04010, doi:10.1029/2008JE003266.
- Wang, A., Z. C. Ling, and J. J. Freeman (2010a), Stability fields and phase transition pathways of ferric sulfates in 50°C to 5°C temperature range, *Lunar Planet. Sci.* [CD-ROM], XXXXI, abstract 2303.
- Wang, A., J. J. Freeman, and J. F. Bell III (2010b), Potential habitable zone within the subsurface of equatorial region on Mars, in *Astrobiology Science Conference 2010* [CD-ROM], *LPI Contrib.*, 1538, abstract 5400.
- Wiseman, S. M., J. L. Griffes, R. E. Arvidson, S. Murchie, F. Poulet, A. T. Knudson, F. P. Seelos, N. Tosca, and the CRISM Science Team (2007), New analyses of MRO CRISM, HiRISE, and CTX data over layered sedimentary deposits in Meridiani, in *Seventeenth International Conference on Mars, July 9–13, 2007, Pasadena CA* [CD-ROM], *LPI Contrib.*, 1353, abstract 3111.
- Yen, A. S., et al. (2008), Hydrothermal processes at Gusev crater: An evaluation of Paso Robles class soils, *J. Geophys. Res.*, *113*, E06S10, doi:10.1029/2007JE002978.

Z. C. Ling, School of Space Science and Physics, Shandong University, Weihai, 264209, China.

A. Wang, Department of Earth and Planetary Sciences, Washington University, St. Louis, MO 63130, USA. (alianw@levee.wustl.edu)